

## Supplementary Materials for

### **A Reconciled Estimate of Ice-Sheet Mass Balance**

Andrew Shepherd,\* Erik R. Ivins,\* Geruo A, Valentina R. Barletta, Mike J. Bentley, Srinivas Bettadpur, Kate H. Briggs, David H. Bromwich, René Forsberg, Natalia Galin, Martin Horwath, Stan Jacobs, Ian Joughin, Matt A. King, Jan T. M. Lenaerts, Jilu Li, Stefan R. M. Ligtenberg, Adrian Luckman, Scott B. Luthcke, Malcolm McMillan, Rakia Meister, Glenn Milne, Jeremie Mouginot, Alan Muir, Julien P. Nicolas, John Paden, Antony J. Payne, Hamish Pritchard, Eric Rignot, Helmut Rott, Louise Sandberg Sørensen, Ted A. Scambos, Bernd Scheuchl, Ernst J. O. Schrama, Ben Smith, Aud V. Sundal, Jan H. van Angelen, Willem J. van de Berg, Michiel R. van den Broeke, David G. Vaughan, Isabella Velicogna, John Wahr, Pippa L. Whitehouse, Duncan J. Wingham, Donghui Yi, Duncan Young, H. Jay Zwally

\*To whom correspondence should be addressed. E-mail: [ashepherd@leeds.ac.uk](mailto:ashepherd@leeds.ac.uk) (A.S.); [erik.r.ivins@jpl.nasa.gov](mailto:erik.r.ivins@jpl.nasa.gov) (E.R.I.)

Published 30 November 2012, *Science* **338**, 1183 (2012)  
DOI: 10.1126/science.1128102

#### **This PDF file includes:**

Materials and Methods  
Supplementary Text  
Figs. S1 to S13  
Tables S2, S4, and S5 to S8  
References

**Other Supplementary Material for this manuscript includes the following:**  
available at [www.sciencemag.org/cgi/content/full/338/6111/1183/DC1](http://www.sciencemag.org/cgi/content/full/338/6111/1183/DC1)

Tables S1, S3, S9 and S10

# Supporting Online Material for A Reconciled Estimate of Ice Sheet Mass Balance

---

Andrew Shepherd<sup>1</sup>, Erik R. Ivins<sup>2</sup>, Geruo A<sup>3</sup>, Valentina R. Barletta<sup>4</sup>, Mike J. Bentley<sup>5</sup>, Srinivas Bettadpur<sup>6</sup>, Kate H. Briggs<sup>1</sup>, David H. Bromwich<sup>7</sup>, René Forsberg<sup>4</sup>, Natalia Galin<sup>8</sup>, Martin Horwath<sup>9</sup>, Stan Jacobs<sup>10</sup>, Ian Joughin<sup>11</sup>, Matt A. King<sup>12</sup>, Jan T. M. Lenaerts<sup>13</sup>, Jilu Li<sup>14</sup>, Stefan R. M. Ligtenberg<sup>13</sup>, Adrian Luckman<sup>15</sup>, Scott B. Luthcke<sup>16</sup>, Malcolm McMillan<sup>1</sup>, Rakia Meister<sup>8</sup>, Glenn Milne<sup>17</sup>, Jeremie Mouginot<sup>18</sup>, Alan Muir<sup>8</sup>, Julien P. Nicolas<sup>7</sup>, John Paden<sup>14</sup>, Antony J. Payne<sup>19</sup>, Hamish Pritchard<sup>20</sup>, Eric Rignot<sup>18,2</sup>, Helmut Rott<sup>21</sup>, Louise Sandberg Sørensen<sup>4</sup>, Ted A. Scambos<sup>22</sup>, Bernd Scheuchl<sup>18</sup>, Ernst J.O. Schrama<sup>23</sup>, Ben Smith<sup>11</sup>, Aud V. Sundal<sup>1</sup>, Jan H. van Angelen<sup>13</sup>, Willem J. van de Berg<sup>13</sup>, Michiel R. van den Broeke<sup>13</sup>, David G. Vaughan<sup>20</sup>, Isabella Velicogna<sup>18,2</sup>, John Wahr<sup>3</sup>, Pippa L. Whitehouse<sup>5</sup>, Duncan J. Wingham<sup>8</sup>, Donghui Yi<sup>24</sup>, Duncan Young<sup>25</sup>, H. Jay Zwally<sup>26</sup>

## Contents

§1. Supporting Data and Figure.....	5
§ 1.1 Published Geodetic Estimates of Ice Sheet Mass Balance .....	5
§ 1.2 Inter-comparison of Geodetic Estimates of Ice Sheet Mass Balance .....	5
§ 1.3 Cumulative Ice Sheet Mass Change .....	6
§2. Definition of Ice Sheet Drainage Divides.....	7
§2.1 Antarctic Ice Sheet Drainage Divides .....	8
§2.2 Greenland Ice Sheet Drainage Divides.....	10
§3. Surface Mass Balance Evaluation and Uncertainties .....	10
§4. GIA Models.....	14
§4.1 Greenland GIA models.....	15
§4.2 Integration of new data.....	15

§4.1.1 Synopsis of the W12a Model Approach and Results .....	16
§4.1.2 Synopsis of the IJ05_R2 Model Approach and Results .....	17
§4.2 Computation of GIA: IJ05_R2 and W12a.....	19
§4.2.1 Model background.....	19
§4.2.2 Model calibration.....	20
§4.2.3 GRACE correction .....	21
§5. Radar Altimetry Methods.....	24
§5.1 Cross Calibration of Satellite Sensors .....	26
§5.2 Density model.....	26
§5.3 Surface Mass Balance.....	28
§ 6. Laser Altimetry Methods.....	28
§ 6.1 GIA correction.....	29
§ 6.2 Bias correction.....	29
§ 6.3 Volume-to-mass conversion.....	30
§ 6.4 BS volume-change estimates.....	31
§ 6.5 HP volume-change estimates .....	32
§ 6.6 SF volume-change estimates .....	32
§ 6.7 YZ volume-change estimates .....	33

§ 6.8 Results .....	33
§ 6.8.1 Volume-change estimates.....	33
§ 6.8.2 Mass-change estimates .....	34
§ 7. IOM Methods .....	35
§ 7.1. Flux gates .....	35
§ 7.2. Ice thickness data.....	35
§ 7.3. Ice velocity data.....	35
§ 7.4. Ice discharge.....	36
§ 8 GRACE Methods .....	37
§ 9 References .....	41

## §1. Supporting Data and Figure

### § 1.1 Published Geodetic Estimates of Ice Sheet Mass Balance

Previously published geodetic estimates of ice sheet mass balance are summarised in Table S1. In total there have been 79 estimates of Greenland and Antarctic Ice Sheet mass balance from 29 publications dating back to 1998. These provide over twice as many estimates of the mass balance of the GrIS as compared to the AIS. These estimates span the period 1958 to 2010 and range between -246 Gt/yr and +27 Gt/yr for Antarctica, and between -308 Gt/yr and +10 Gt/yr for Greenland.

Table S1. Published mass balance estimates of the Greenland and Antarctic Ice Sheets derived using Altimetry, Gravimetry and IOM methods. Where only volume change was reported in the literature, a conversion to  $dm/dt$  has been made (95) using either the density of ice or water as indicated in the published articles. \*(grounded ice) † (floating ice). See additional Excel Spreadsheet: Tables S1 S3 S9 S10.

### § 1.2 Inter-comparison of Geodetic Estimates of Ice Sheet Mass Balance

Estimates of ice sheet mass balance determined using the individual satellite geodetic techniques over a common time period are presented in Table S2. None of the ice sheet sector (GrIS, APIS, EAIS, and WAIS) mass balance estimates derived from the individual techniques depart significantly from the mean value, given the respective uncertainty of the measurements. Once integrated, only the laser altimeter estimate of the combined GrIS and AIS ice sheet mass imbalance departs significantly from the mean estimate and, at  $140 \pm 133 \text{ Gt yr}^{-1}$ , the departure is only marginally beyond the 1-sigma uncertainty range of the respective values. Nevertheless, there are noteworthy patterns in the distribution of mass balance estimates that warrant further discussion. The radar altimeter and GRACE estimates of mass balance are in general close, and closest to the mean estimate of mass balance in the regions where both measurements coincide. The laser altimeter estimates of ice sheet mass balance are generally higher (more positive) than all other estimates. The input output method estimates of ice sheet mass balance are generally lower (more negative) than all other estimates. Despite these patterns, there is no evidence to support the existence of a systematic bias between the measurement techniques, given their respective uncertainties. The relatively large variance between the individual estimates of ice sheet mass balance can be attributed mainly to the relatively short time period of the observations, during which (i) fluctuations in surface mass balance are typically large and, consequently, relatively difficult to characterise, and (ii) uncertainties of trends derived from the geodetic measurements themselves are relatively large also.

Table S2. Ice sheet mass balance estimates determined using the individual satellite geodetic techniques of the input-output method (IOM), radar altimetry (RA), laser altimetry (LA), and gravimetry, and over the period October 2003 to December 2008 during which all techniques were in operation. Also shown is the arithmetic mean of each individual result available for a given region, and the combined imbalance of the AIS and the AIS plus the GrIS, calculated as the sum of estimates from the constituent regions.

Region	IOM mass balance (Gt/yr)	RA mass balance (Gt/yr)	LA mass balance (Gt/yr)	Gravimetry mass balance (Gt/yr)	Average mass balance (Gt/yr)
GrIS	-284 ± 65	-	-185 ± 24	-228 ± 30	-232 ± 23
APIS	-36 ± 17	-	-28 ± 18	-21 ± 14	-28 ± 10
EAIS	-30 ± 76	22 ± 39	109 ± 57	35 ± 40	24 ± 36
WAIS	-77 ± 38	-54 ± 27	-60 ± 39	-68 ± 23	-67 ± 21
AIS	-142 ± 86	-	21 ± 81	-57 ± 50	-72 ± 43
GrIS + AIS	-427 ± 108	-	-164 ± 84	-285 ± 80	-304 ± 49

### § 1.3 Cumulative Ice Sheet Mass Change

Cumulative curves of ice sheet mass change as determined by individual geodetic techniques are presented in Fig. S1

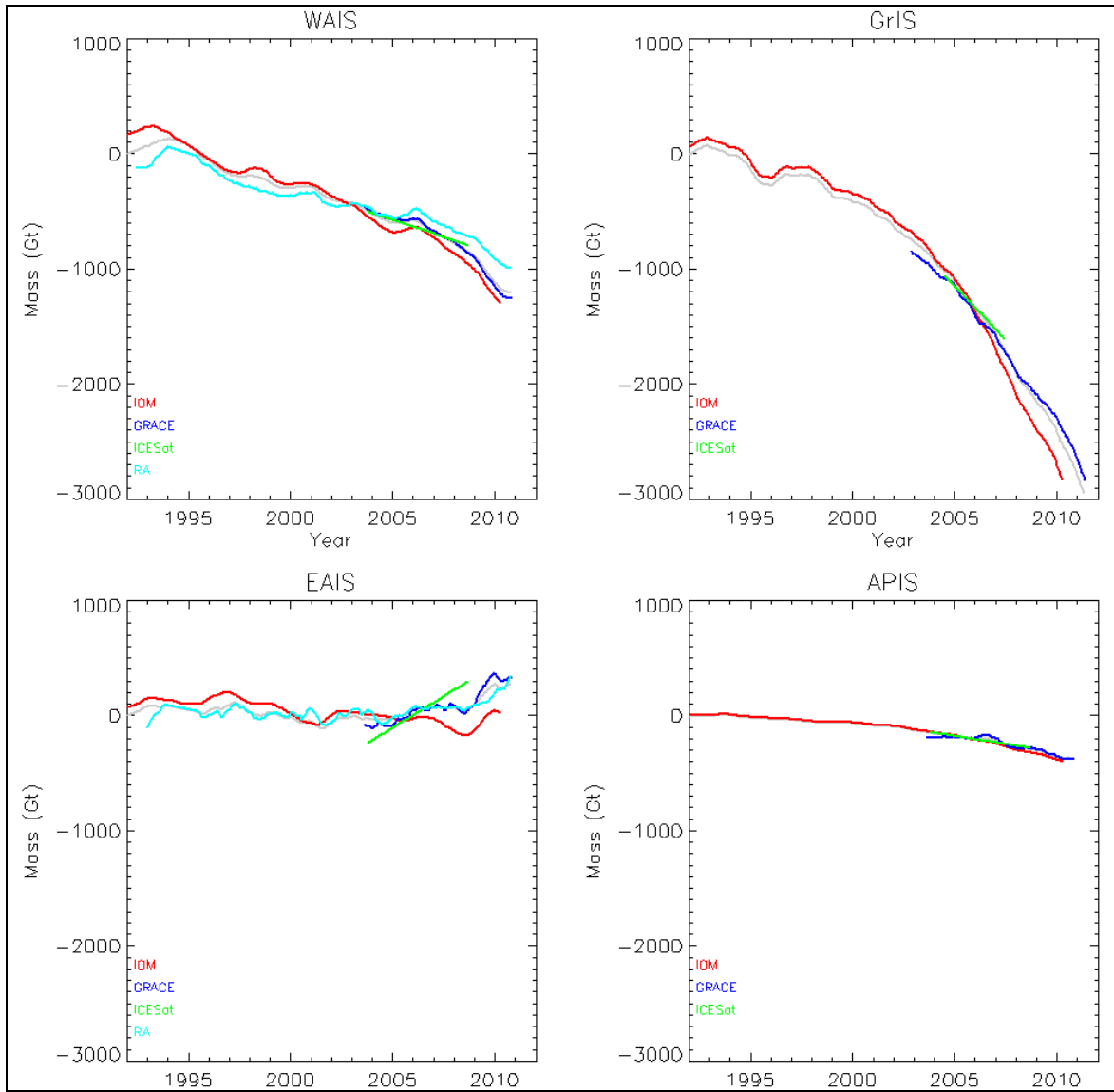


Figure S1. Cumulative ice mass change of West Antarctica, East Antarctica, Greenland and the Antarctic Peninsula (WAIS, EAIS, GrIS and APIS respectively), as observed by the Input-Output Method (IOM), GRACE, ICESat and Radar Altimetry (RA). Each time-series is offset so that the observed mean cumulative mass matches that of our reconciled estimate over the same period (Fig. 5). A 13-month moving average is applied to the IOM, RA, and GRACE data.

## §2. Definition of Ice Sheet Drainage Divides

The definition of ice sheet drainage divides is an important consideration when developing estimates of ice sheet mass balance. Satellite altimeter estimates of mass balance are typically determined by integrating measurements of elevation changes that fall within the lateral extent of the ice sheet. IOM estimates of ice sheet mass balance are typically determined by integrating estimates of surface mass balance that fall within the lateral extent of the ice sheet, and then subtracting the ice discharge that is transported

across the boundary. In some cases, it is not possible to compute estimates of ice transport across the true boundary, and so an alternative flux gate is defined elsewhere, leading to an error associated with the omission of measurements. Satellite gravimetry estimates of ice sheet mass balance are typically determined by integrating measurements of gravity fluctuations occurring within a region that is larger than the ice sheet lateral extent, to account for the relatively low spatial resolution of the sensor. Accuracy (or consistency) in the definition of ice sheet lateral extents is of most importance when developing estimates of mass balance using the technique of satellite altimetry or the input-output method.

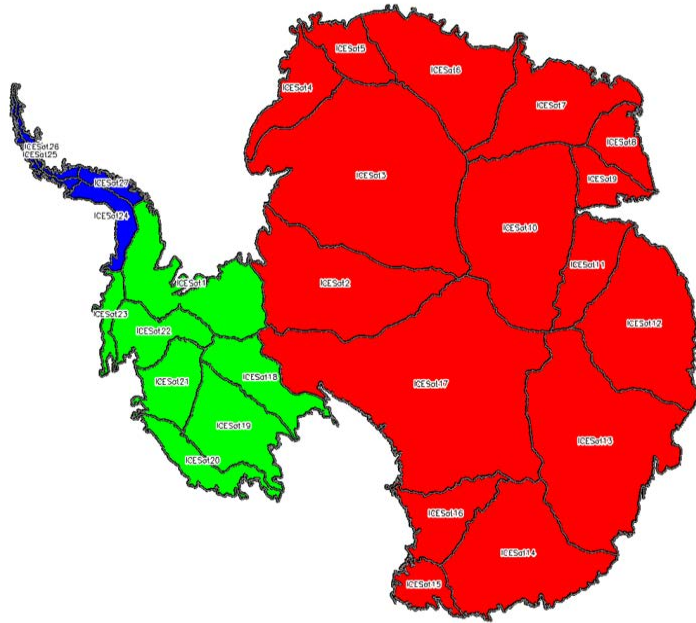
A principle objective of this study was to develop estimates of ice sheet mass balance using common spatial and temporal domains. To achieve this objective, we attempted, where possible, to utilise common definitions of the lateral extents of ice sheet sectors. In the case of the Antarctic Ice Sheet sectors, all groups utilised common definitions of the ice sheet lateral extent when aggregating their geodetic datasets. The relatively small size of the Greenland Ice Sheet did, however, preclude such an approach. Instead, a variety of definitions were employed to delineate the lateral extent of the ice sheet. In the following sections we describe the detailed definitions employed in this study.

## §2.1 Antarctic Ice Sheet Drainage Divides

Historically, drainage sectors and the division of the Antarctic Ice Sheet into East, West and the Peninsula have been based on the original definition of (111) (e.g. (55,59)). Using a 111 km resolution DEM and hand drawn flow lines that were produced by (112), (111) segmented the AIS into 26 physiographically distinct sectors. This definition centred on the initial separation of the ice sheet into six major sectors, identified on the basis of the routing of ice to major ice shelves or the periphery of the continent. Subsequent redefinitions and classifications of the AIS sectors as components of the EAIS, WAIS and APIS have also been based on the location of the glacier outlets (e.g. (55)). However, the most recently produced map of AIS drainage sectors by (113) offers an alternative basis for defining the EAIS, WAIS and AP. Using a 500 m resolution DEM derived from ICESat observations they identified 27 drainage sectors (113). These sectors were assigned to the EAIS, WAIS and APIS based on the provenance (rather than the destination) of the ice, and their definition divides the EAIS and WAIS along the Trans-Antarctica Mountains (Fig. S2).

The map of (113) was chosen as the primary basin map for this project on the basis that it offers the most recent sector definitions and a preferred division of the EAIS and WAIS. All gravimetry and altimetry results reported here have used the (113) basin definitions. The reported IOM results for Antarctica were calculated using the basin map of (55). By comparison to the map of (113), the map in (55) includes a larger number (65) of smaller basins. The basins in (55) have been grouped to match the basins in (113) as closely as possible in Table S3. For this project the segregation of the AIS into East, West and the Peninsula according to (55) was modified so that the Foundation Glacier basin was included within East Antarctica, thereby maintaining consistency with (113) (Fig. S2 a&b).

A)



B)

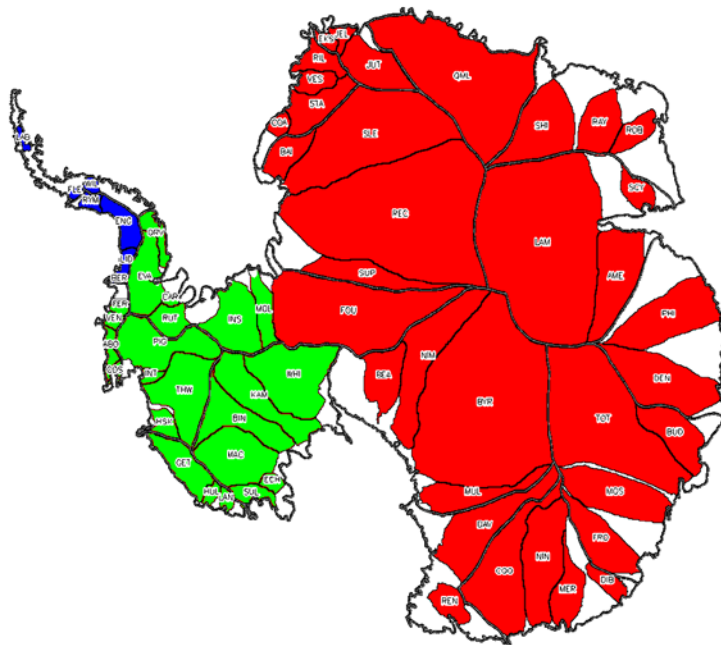


Figure S2. A) The most recent definition of AIS basins by (113) based on a 500 m resolution ICESat DEM and including 27 sectors. The division of the ice sheet into the EAIS, WAIS and APIS are shown in red, green and blue respectively. B) The 65 drainage basins of (55) and their assignment to the EAIS, WAIS and APIS (colours as in A). Note that FOU is now included in WAIS. The white areas in this map indicate regions of ice not included within the survey and referred to as “omission areas” in the text. Basin name abbreviations are as used by (55).

Table S3. The drainage basins of (55) as assigned to the drainage sectors of (113) and the EAIS, WAIS and APIS regions used within this project. Basin name abbreviations are as used by (55). See additional Excel Spreadsheet: Tables\_S1\_S3\_S9\_S10.

## §2.2 Greenland Ice Sheet Drainage Divides

A range of commonly accepted definitions exist for the lateral extent of the Greenland Ice Sheet. In this study, it was not possible to use identical domains for this ice sheet due to the manner in which low-level datasets from the groups involved have been historically developed. Instead, three different sets of Greenland Ice Sheet drainage divides were employed; two during the calculation of satellite altimetry estimates of mass balance, and a further one during the calculation of input output method estimates of mass balance. The average area of the three Greenland Ice Sheet classification schemes was  $1,709,420 \pm 32,273 \text{ km}^2$ .

A first satellite altimetry estimate of Greenland Ice Sheet mass balance was computed using a definition of the ice sheet lateral extent based on ICESat altimetry (113) drawn on surface vector maps derived from the 1-km DEM of Greenland developed from ICESat/GLAS data (114; 115). This definition resulted in the identification of 19 separate drainage basins, with a combined area of  $1,722,572 \text{ km}^2$ . A second satellite altimetry estimate of Greenland Ice Sheet mass balance was computed using a definition of the ice sheet lateral extent based on a cartographic land classification scheme (116). This definition resulted in the identification of an ice sheet with an area of  $1,672,650 \text{ km}^2$ , and an area of surrounding ice caps of  $98,600 \text{ km}^2$ , yielding a combined ice covered area of  $1,771,250 \text{ km}^2$ .

Input-output method estimates of Greenland Ice Sheet mass balance were computed using a definition of the ice sheet lateral extent based on the delineation of 84 discrete glacier drainage systems (18). These drainage systems are defined relative to flux gates where ice thickness data are available for the computation of ice discharge, extended to the ice position of glacier fronts as defined in satellite imagery. The combined area of these basins is  $1,610,266 \text{ km}^2$ , and mass imbalance from intervening regions is estimated using an extrapolation scheme (see Section 7.4), leading to an overall survey area of  $1,733,044 \text{ km}^2$ .

## §3. Surface Mass Balance Evaluation and Uncertainties

SMB estimates for the AIS and GrIS are from the RACMO2 Regional Atmospheric Climate Model (22) over the period 1979 to 2010, with horizontal resolution of 27 km (AIS) and 11 km (GrIS). We distinguish spatial and temporal uncertainty in SMB

estimates. The spatial uncertainty of RACMO2 accumulation (total precipitation minus sublimation) has been assessed through comparison with 310 (GrIS) and 1850 (AIS) in-situ accumulation observations, mostly from shallow to medium-deep firn cores with a well-dated horizon. The procedure allows for measurement uncertainties in the observations, and iteratively searches for the accumulation uncertainty in the model output, assuming that the difference between model and observations is normally distributed (28). To go from an uncertainty estimate for accumulation to that in SMB, the uncertainty in meltwater runoff must be quantified. Runoff is very small on the AIS, and its contribution to the uncertainty in the SMB is neglected. For the GrIS, no direct runoff estimates are available, and a constant uncertainty of 20% to modelled runoff has been assigned.

Because snowfall fluctuations are poorly resolved in observational datasets, the temporal SMB uncertainty is assessed through comparison of RACMO2 with global atmospheric reanalyses (16). We only do this for the AIS, because the GrIS topography and hence SMB is poorly resolved in coarse-gridded GCMs. Our assessment of the temporal uncertainty in AIS SMB is based on a comparison between SMB data from RACMO2 and those from three global reanalyses: the European Center for Medium-range Weather Forecasts (ECMWF) ERA-Interim (117), which is also used to drive the boundary conditions of RACMO2 (61); the National Centers for Environmental Prediction (NCEP) Climate Forecast System Reanalysis (CFSR) (118); and the National Aeronautics and Space Administration (NASA) Modern Era Retrospective-Analysis for Research and Applications (MERRA) (119). For the three reanalyses, SMB is approximated as precipitation-minus-surface sublimation (P-S), which neglects other SMB components simulated by RACMO2, such as drifting snow processes and meltwater runoff. These additional terms, however, represent less than 7% of the integrated SMB in Antarctica and show little temporal variability (61). This variability is therefore well accounted for by P-S.

As previously shown (19), the results from a regional climate model simulation are influenced by its driving reanalysis. This also implies that the regional simulation may be subject to the same problems as those present in the reanalysis. With regards to the temporal variability, the most important issues relate to changes in the observations assimilated into the reanalysis and may be manifested as discontinuities or spurious trends in some atmospheric fields (120-122). When they occur, such issues are often particularly pronounced over the Southern Ocean (the moisture source for Antarctic precipitation) given the extreme sparsity of conventional observations in this area. These problems have been found (to various degrees) in all contemporary global reanalyses, including ERA-Interim (117, 123), CFSR (118,122,124), and MERRA (122,125,126). Owing to a spurious sharp increase in precipitation in MERRA over the Southern Ocean in the late 1990s/early 2000s, we do not use data from this reanalysis prior to January 2003 (MERRA is used only in Fig. 2, not in the supporting figures and table discussed below). Similarly, because the precipitation fields from the other reanalyses may be affected by the introduction of the SSM/I observations in 1987, we do not use data from ERA-Interim nor CFSR prior to January 1989.

Fig. S3 shows the cumulative SMB anomalies derived from RACMO2, ERA-Interim, and CFSR for the three main Antarctic regions. Cumulative anomalies are used here as they represent the input term in the IOM, when this method is compared to GRACE (see

Fig. S1). Further details on the methodology are provided in the supplementary information from (5). Since the complex topography of the APIS is not necessarily well captured by the model grid resolutions (ranging from ~38 km in CFSR to ~80 km in ERA-Interim), the results for this region (Fig. S3c) should be interpreted with caution. We note that, on scales of a few years, the three datasets are often highly correlated with each other. The uncertainty of the trends in the SMB product was estimated, as in ref. (5), by varying the baseline period used to compute the anomalies. A total of twenty 20-year baseline periods were randomly selected within 1980-2010, yielding 20 sets of anomalies, cumulative anomalies, and trends per dataset and per Antarctic region. In each instance, the trend uncertainty was estimated as two standard deviations ( $2\sigma$ ) of the 20 trend values. The overall trend and uncertainty for each region were finally calculated as the average of the values obtained with the three datasets, i.e., the average trend as the arithmetic average of the trends, and the average uncertainty as the root mean square of the average of the squared uncertainties. The envelopes of cumulative SMB anomalies generated with this method are shown in Fig. S3. The corresponding trend/uncertainty values are shown in Table S4.

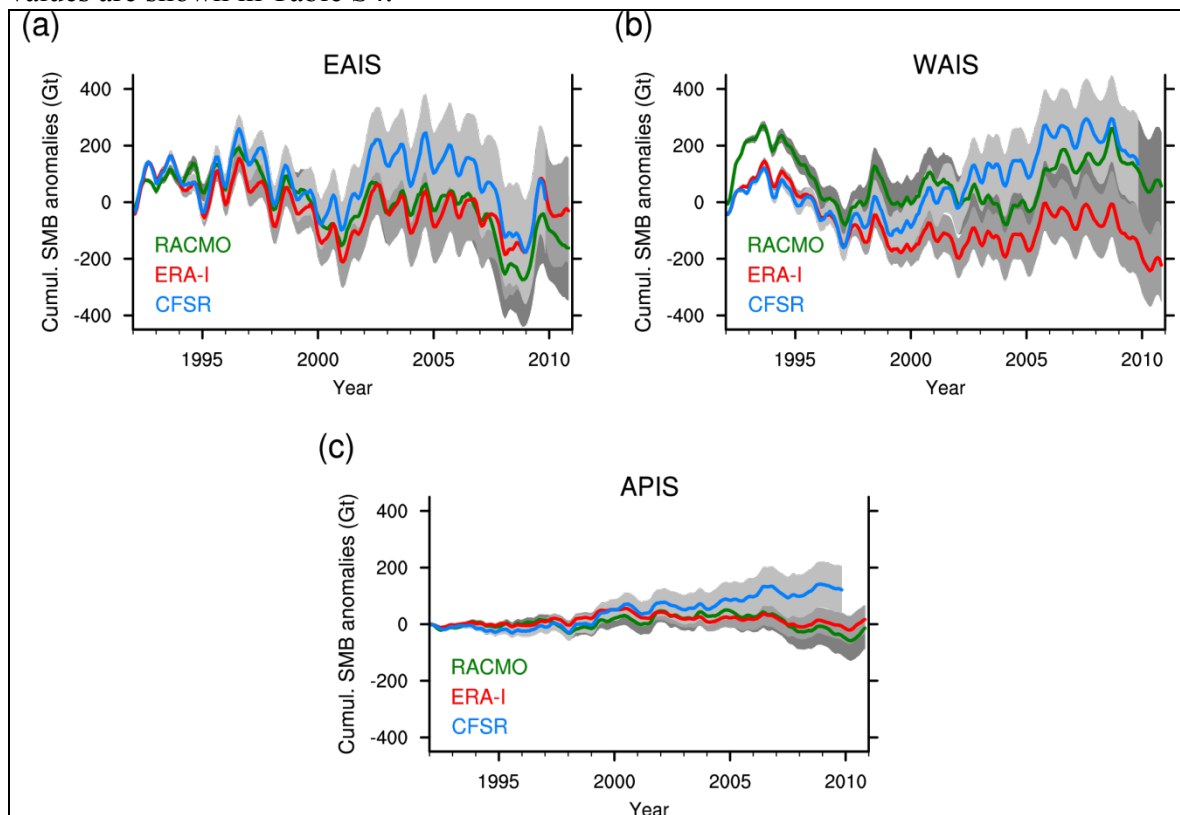
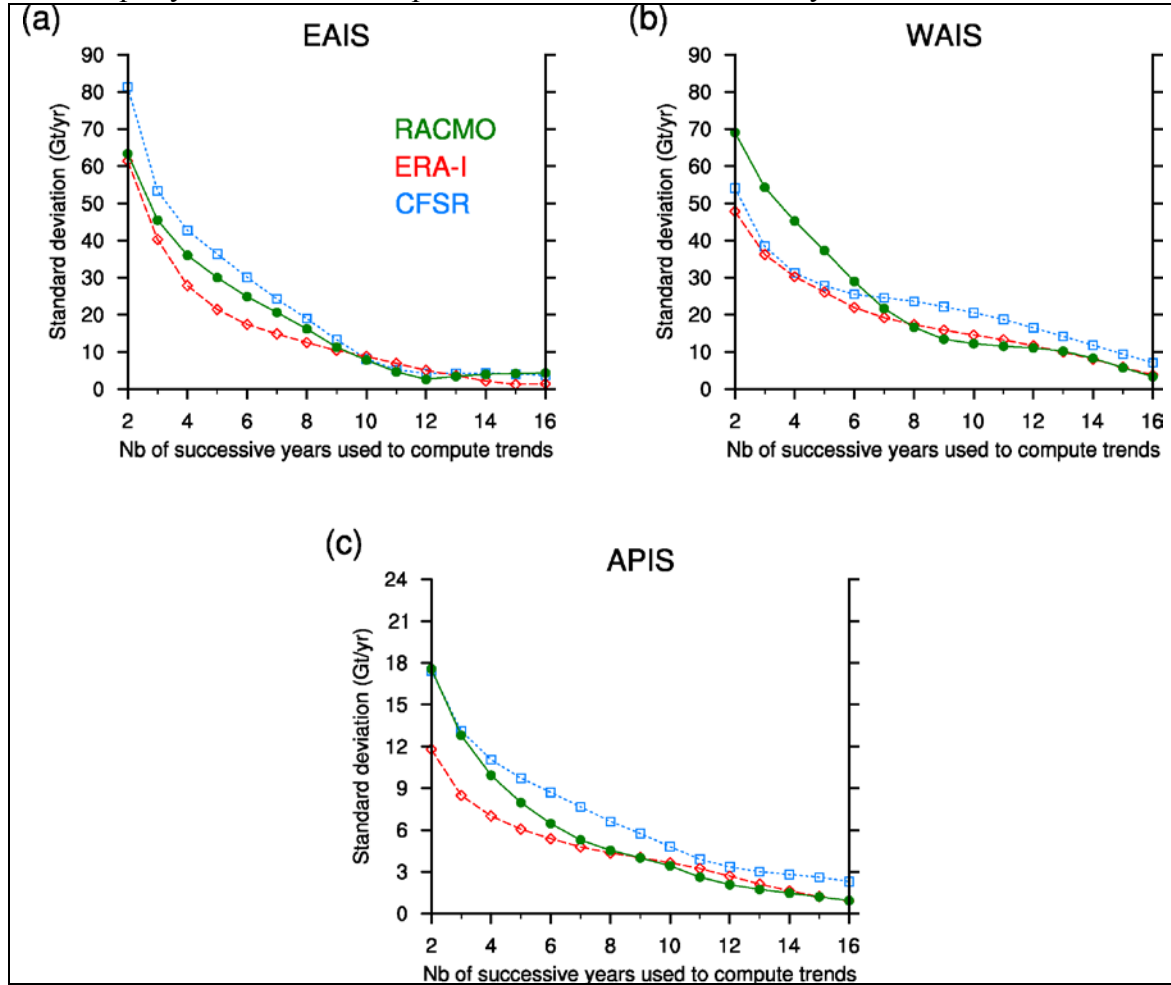


Figure S3. Monthly cumulative SMB anomalies in Gt for the three Antarctic regions from RACMO2 (green), ERA-Interim (red), and CFSR (blue). The grey shaded envelopes (one shade per dataset) represent the different sets of cumulative anomalies generated by varying the baseline period (see details in the text). The coloured lines represent the respective means of the three envelopes. A three-month running average is applied to the time series.

The large inter-annual variability in snow accumulation is an additional source of uncertainty to consider when assessing the trends in Antarctic SMB. This variability is

clearly apparent in Fig. S3 and has been documented in a number of studies (61,122,127). It is also illustrated in the regional case study presented in Fig. 2. It follows that trend values are highly sensitive to the length of the period over which they are calculated (Fig. S4). Notably, despite some inter-model differences, Fig. S4 shows that the range of the trends rapidly increases for temporal windows shorter than 10 years.



FigureS4. Standard deviations of the trends in cumulative SMB anomalies (Gt/yr; y-axis) calculated for different temporal windows (years; x-axis) within the 1989-2010 period. The results are shown for EAIS (a), WAIS (b), and APIS (c) using monthly cumulative SMB anomalies from RACMO2 (green), ERA-Interim (red), and CFSR (blue) (these cumulative anomalies are those shown in Fig. S3). Note that the number of trend values used to calculate the standard deviations decreases as the number of years increases (e.g., 21 values for 3-year windows; 7 values for 16-year windows).

Table S4. Trends in cumulative SMB anomalies for the three Antarctic regions from RACMO2, ERA-Interim, and CFSR. For each dataset and region, the uncertainty ( $\pm 2\sigma$ ) was estimated by varying the baseline period used to compute the SMB anomalies (see details in the text). The trends are shown for two periods: Oct. 2003 – Dec. 2008 (as in Table S1); and Jan. 1992 – Dec. 2009 (same start year as Table 1, col. 2). For the ‘mean’, the trend represents the arithmetic average of the values derived from the three datasets. The average uncertainty is calculated as  $\sqrt{(\frac{1}{3}\sum 4\sigma^2)}$ .

Model	Trends in cumulative SMB anomalies (Gt/yr)					
	Period: 10/2003 – 12/2008			Period: 01/1992 – 12/2009		
	EAIS	WAIS	APIS	EAIS	WAIS	APIS
RACMO2	-55 ± 20	55 ± 20	-13 ± 8	-14 ± 20	0 ± 20	1 ± 8
ERA-Interim	-24 ± 20	24 ± 14	-4 ± 6	-9 ± 20	8 ± 14	1 ± 6
CFSR	-58 ± 22	35 ± 18	12 ± 10	-4 ± 22	16 ± 18	10 ± 10
Mean	-46 ± 21	38 ± 18	-2 ± 8	-9 ± 21	8 ± 18	4 ± 8

#### §4.GIA Models

In this section we provide supporting materials to describe and support our choice of the GIA models used for the GRACE and Altimetry components of the analysis. All of the models used for Greenland have been previously published. Hence, in §4.1 we briefly outline the models used for this region. The majority of this section, however, focuses on the GIA models we adopted to provide GIA results for Antarctica - a revised version (R2) of the IJ05 post-glacial rebound model for Antarctica (41) and a new model (W12a) (35) – with most of the discussion focusing on the former since it has not yet been published. Both approaches built upon the work of (41) (i.e., model IJ05\_R0), but they are entirely independent and the W12a model, in contrast to IJ05\_R2, is based on a glaciological model that simulates ice flow dynamics (40) and the Earth model component is calibrated to a regional (Antarctica) relative sea-level data set (35). Both models, and their variants, make use of the existing glacial geological and glaciological data for improved fidelity in time and space of Antarctic ice extent over those of global models, most notably the widely used ICE-5G (v1.2) (39).

In §4.1 we define the GIA models used for Greenland. In §4.2 we briefly outline the new geological and geomorphological data integrated into the revised Antarctic ice history models, and in §4.3 we describe the computation of glacial isostatic adjustment with W12a and IJ05\_R2. Finally, in §4.4 we show how the Antarctic models are constrained using new Global Positioning System (GPS) data and how new corrections for GRACE trends are developed.

It is important to note the difference between GIA and post-glacial rebound (PGR). The term post-glacial rebound (PGR) refers to the land rising back to its position as it was prior to surface loading by an ice sheet. Glacial isostatic adjustment (GIA) is a more

general term that encompasses all of the processes related to the response of the solid Earth to late Quaternary land ice evolution (such as changes in Earth rotation and the geopotential). Given that this process leads to regional land subsidence in many regions at present, including parts of Antarctica, it is appropriate to adopt this more general terminology here.

#### §4.1 Greenland GIA models

We adopt results from three recent studies (36-38). In one of these studies (37), the ice history was calibrated using a single Earth viscosity model and so, in this case, only one ice-Earth model combination was considered: ICE-5G/VM2 (39). In the other two studies (36, 38), results indicated that quality data-model fits were achieved with a small suite of Earth viscosity models for the optimum ice history. We consider these proposed viscosity models to quantify GIA model uncertainty. In both of these studies, the Earth viscosity models were parameterised into three regions: (1) an outer shell of high viscosity to simulate the lithosphere; (2) an upper mantle region of uniform viscosity from the base of the model lithosphere to the 660 km seismic velocity discontinuity and (3) a lower mantle region extending from 660 km depth to the core-mantle boundary. Based on the results in (38), we considered a total of 27 Earth models that sampled the following parameter values: lithospheric thickness,  $h$  (values of 50, 80, 100 km); upper mantle viscosity,  $\eta_{UM}$ : 2, 4,  $5 \times 10^{20}$  Pas; lower mantle viscosity,  $\eta_{LM}$ , (5, 10,  $20 \times 10^{21}$  Pas). An Earth model with the intermediate values of these parameters provided the best fit. Based on the results in (36), we adopted the following eight parameter sets ( $h$  (km),  $\eta_{UM}$  ( $\times 10^{20}$  Pas),  $\eta_{LM}$  ( $\times 10^{21}$  Pas)) that provided equivalent fits (95% confidence) to the relative sea-level data considered: (96/3/2), (96/5/5), (96/5/8), (96/5/10), (96/8/5), (120/5/1), (120/8/1), (120/10/1). Of these eight Earth models, 120/5/1 produced the optimum fit. Thus, the GIA model uncertainty for Greenland is based on a total of 36 ice-Earth model combinations. For information on how these predictions we used to correct the Altimetry and GRACE data, see §5 and §8, respectively.

#### §4.2 Integration of new data

Over the last 8 to 10 years there has been a substantial increase in the number and distribution of new constraints on past changes in Antarctic ice extent. (40) incorporated data from 62 locations, related to the timing and magnitude of past ice height differential values (IHD), into their ice model. The new IJ05\_R2 used data from all of these locations, but did not revise the Antarctic Peninsula history due to the complications of the Little Ice Age (73, 128) and a strong north-south viscosity gradient inferred in this region, with very low viscosity to the northern tip of the Antarctic Peninsula (129). Fig. S5 shows a small sample of the locations of the new data used that are common to both models. Important sites including Mac. Robertson Land (e.g. 45), Talos Dome, Dome Circe ('C') and Dome Fuji, have provided new information on ice retreat, thickness and volume, and rates of thinning and accumulation over the past 21 ka. Full accounting of the data and locations are given in (40), Table 1 and Fig. 1, therein. These new data suggest that the volume of ice at the LGM was considerably smaller than previously thought (45, 130). A major breakthrough in understanding ice thickness changes in East Antarctica came from detailed snow accumulation modelling of ice core annual layers. In the Talos Dome region, for example, estimates suggest that the maximum ice sheet

elevation was reached between 17.0-12.7 ka and diminished to present-day values by 7 ka, the total variation being limited to roughly 170 meters of positive IHD (e.g., (131), Table 5 therein).

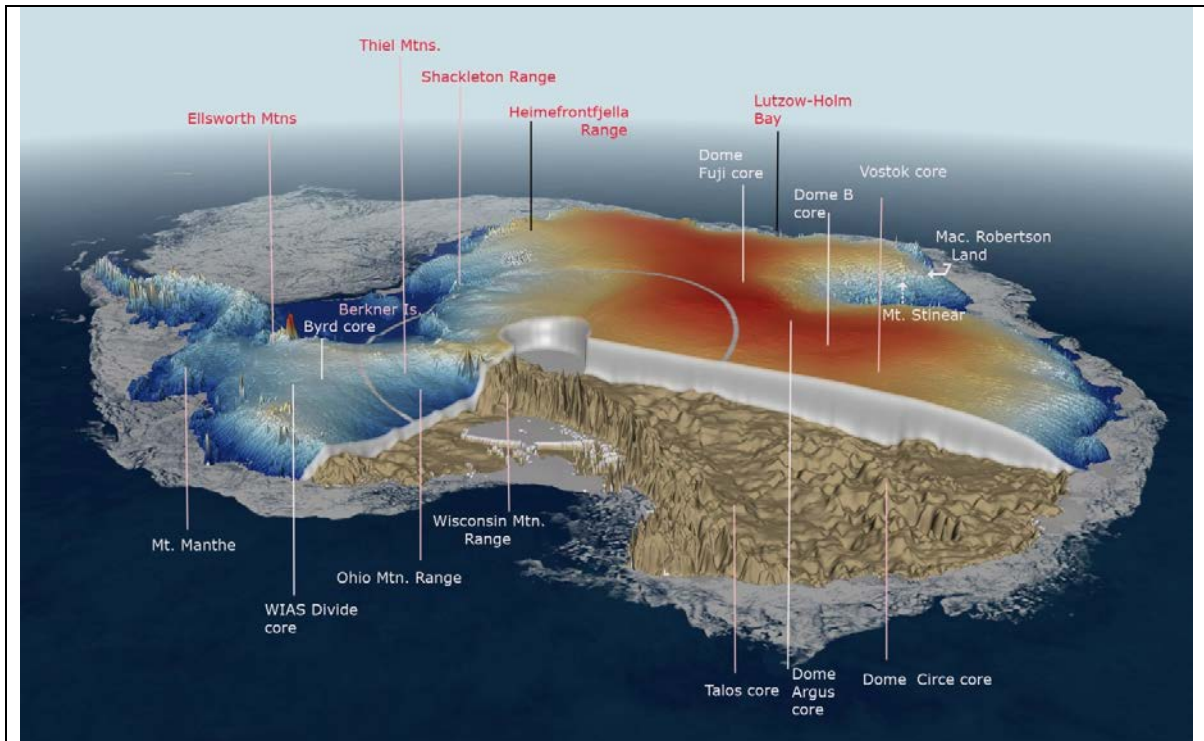


Figure S5. Cut-away of the Antarctic ice sheet from recent CryoSat data with bottom topography and sea ice. Some  $^{10}\text{Be}$ -dated sites are shown where new geochronological constraint data have been derived (post-IJ05). Ice core locations that contribute to accumulation and ice divide migration constraints are also shown. (Image credit: CPOM/UCL/ESA/Planetary Visions, 2012).

While the two new ice models (W12a and IJ05\_R2) use largely the same data as constraints, the two are formulated in entirely different ways. The model approaches are briefly summarized here, but the reader should consult (41,132-133) for greater detail on IJ05\_R2 and (35,40,134) for greater detail on W12a.

#### §4.1.1 Synopsis of the W12a Model Approach and Results

The approach by (35,40) has the following essential components:

- Used a three-dimensional, time-dependent, shallow-ice approximation code that is documented by (135).
- Initialization used a 50 ka spin-up so that near-equilibrium was achieved for the Last Glacial Maximum (20 ka)
- Basal sliding parameters of the model were varied in a series of model runs, developing an ensemble suite, from which ‘best-fitting’ models could be determined (also see (134)).

- A series of five masks defining the model boundaries (ice sheet grounding lines) were developed for time-slices 20, 15, 10, 5 and 0 ka, on the basis of marine geological data from the continental shelf (e.g., (136)).
- The numerical ice sheet model was used to determine transient ice sheet configurations for the post-LGM time-slices listed above, and linear interpolation was used to generate 1 ka time-slices for input into the GIA calculations. Ice load changes outside the Antarctic Peninsula were set to zero after 2 ka.
- The definition of a ‘best-fit’ model run included both comparisons to the IHD data inferences from glaciological geological records and to the present-day ice sheet surface heights.

While a flexural rigidity with a single relaxation time was used to approximate mantle plus lithosphere behaviour in order to compute the vertical position of the Earth’s crust at each time step when developing the ice model of (40), the calculations in a second part of this study used the ‘best-fit’ ice models and a wider range of Earth structure models in an attempt to match relative sea-level (RSL) data time-series at 8 sites on the continent and 6 sites in the Antarctic Peninsula. Nearly 300 Earth structure models were run varying upper mantle and lower mantle viscosity and lithospheric thickness, in an attempt to determine the optimum fit to the RSL data.

As described in (35), a modification was made to the final 1 ka of Antarctic Peninsula ice history to better fit the GPS trend data at sites on the Antarctic Peninsula, after correcting for elastic effects using the mass flux elastic model of (34).

The main outcome is that a single, optimum ice model, W12a, could be derived and has been generated by use of numerical ice sheet modelling and data assimilation.

#### §4.1.2 Synopsis of the IJ05\_R2 Model Approach and Results

The methods used for IJ05\_R2 have evolved from the work described in (132) and (41). However, these are considerably less refined than those employed by (35,40), although both models adhere to the glacial geological data constraints. There are sufficient differences between the two approaches for an inter-comparison of resultant GIA-corrections for GRACE analysis of mass balance trends to be indicative of the whether or not the new models produce a clear improvement in the correction. The following are the main IJ05\_R2 assumptions that differ from those of W12a:

- The model is ‘quasi-static’ in that the model lacks both flow dynamics and explicit accumulation flux, though the temporal variability of the latter is accounted for.
- The grids are formed by 455 spherical caps of varying radii. The height of each cap is the estimated IHD, with isostatic adjustment approximated as fractional values of isostatic equilibrium. Over land that is presently covered by ocean or an ice shelf, loads are set to zero if, at the time of maximum glacial extent, the grounded ice mass did not exceed a value sufficient to have produced an incrementally larger radial stress at the ice-bedrock interface. Calculations by (133) show this to be a fairly accurate approximation.
- Where available, geochronological data, and past grounding line position data, are applied directly to each grid at nine times after the LGM (assumed to be 21 ka).

(The time slices in IJ05\_R2 may be seen in Fig. S6). Linear extrapolations are applied to time periods when no chronological data exists, and further linear interpolations are used to decimate the model into 1 ka increments for the purposes of GIA runs. The model is terminated at 1 ka, and all IHD values are set to zero at this model time.

- The model reconstruction is biased to large IHD values at each of the 10 time slices (including the LGM). The bias allows interpretation of the model as maximum in volume among competing ice forward models that obey the constraints provided by the IHD data. In Mac. Robertson Land, many of the IHD constraints are located within 100 km of one another, and each may be discrepant by a factor of 2, or more. Because of this, we bias the cap-approximated grid estimate to the largest positive IHD value.
- Regions that lie far from the coastline of East Antarctica and from ice core sample locations are poorly constrained in IHD value, and hence, poorly constrained in volume. For these regions ice domes, and not depressions, reaching ice flow equilibrium values are assumed. No massive (kilometre thick, or thicker) ice domes supported by accumulation are inferred in this extrapolation, as flow and accumulation modelled ice core data do not support such LGM dome formation anywhere in Antarctica (137-141).

Far-field post-glacial relative sea-level studies, such as those incorporated into the global analysis in the ICE-5G model by (39), use the Antarctic Ice Sheet (AIS) as the primary southern hemispheric source for model continent-to-ocean water mass exchange. Similarly, a large Antarctic component of melt-water is assumed in the far-field regional analyses of (142) using the ANU series of models. The total AIS exchange in such models is two to three times larger than that inferred from the models of (35) and (40), and IJ05\_R2. Fig. S6 shows the melt-water transport in eustatic sea level equivalent as a function of time, sourced from the Antarctic continent and continental shelf above the ice freeboard. We also show the model published in (45), denoted M11. There is fairly discrepant total transfer at any given time slice among W12a, IJ05\_R2 and M11. In fact, the ensemble simulations that deviated from the IHD data by less than  $1-\delta$  may have 3-meter level differences in total water transfer, owing to uncertainties in the IHD constraint data (35,40). A comparison of the ICE-5G AIS PGR-load at 20 and 9 ka reveals that it is a factor of 2.1 and 3.3 times larger than the nearest competing models, respectively. Each of the competing models (W12a, M11, IJ05\_R2) incorporate the  $^{10}\text{Be}$ ,  $^{26}\text{Al}$  exposure dating of glacial erratics that form the backbone of the new constraints on IHD that are not included in ICE-5G. For a comprehensive review of the details of this type of analysis we refer the reader to (143).

It cannot be overemphasized how different the new models are from ICE-5G: the most remarkable difference between the new and old models is revealed in Fig. S6 at 9-10 ka between ICE-5G, and W12a, the former ice load being 13 times larger than the latter at this time. The reduction in total AIS mass loss in comparison to the Antarctic component of existing global models (ICE-nG and ANU series) will force adjustments to future global sea-level models.

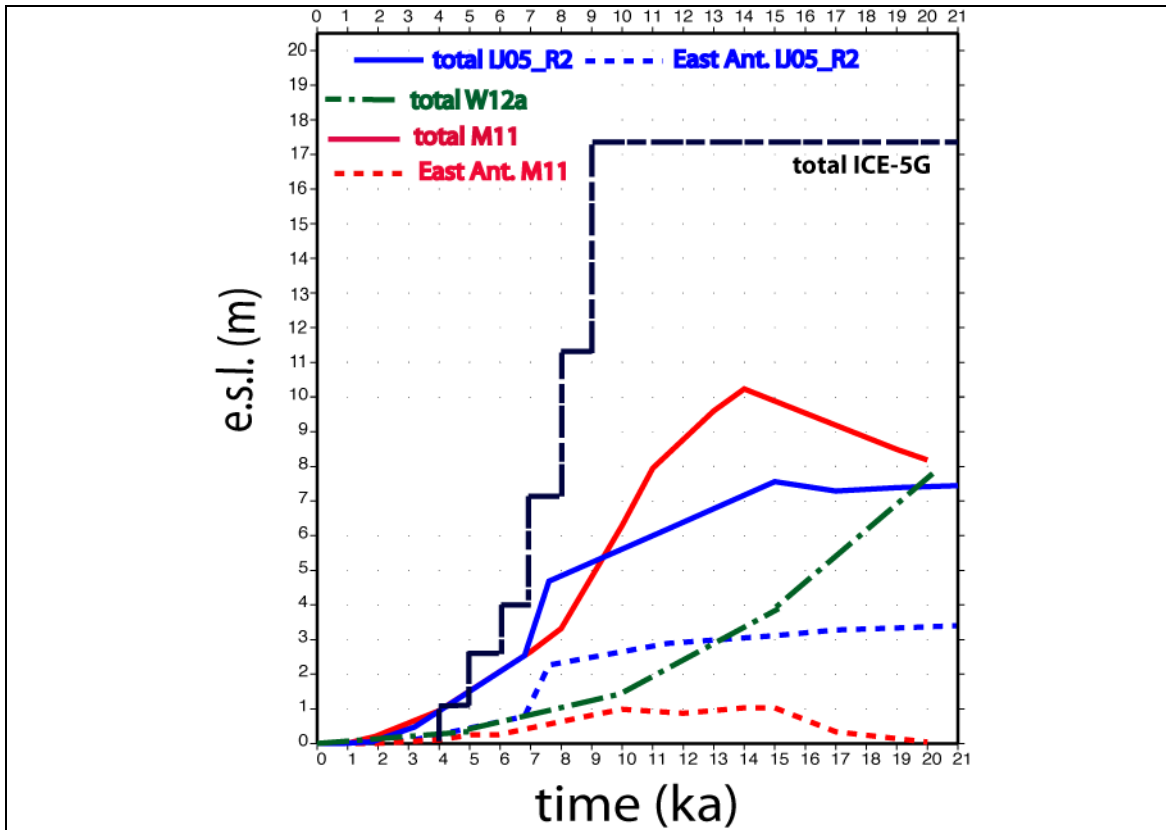


Figure S6. Excess AIS volume (relative to present) in terms of eustatic equivalent sea-level (e.s.l.). (For example, the excess volume increases in the M11 model by about 2 meters e.s.l. between 20 and 14 ka). M11 is the model published in (45). W12a is the (35,40) model and IJ05\_R2 is the model of Ivins *et al.*, described here. Only the ICE-5G model, used in many Antarctic GRACE studies for PGR-correction, does not use the recent geological constraint data. Note that large discrepancies remain between models that incorporate the new geochronological data, although all are substantially reduced in the melt-water component in comparison with ICE-5G.

## §4.2 Computation of GIA: IJ05\_R2 and W12a

### §4.2.1 Model background

For the computations of the predictions of Earth response to the IJ05\_R2 load history model, a spherical code with ocean loading and self-gravitation for a layered mantle has been used. The model is incompressible, has a fluid stratified core, uses a Maxwell viscoelastic linear rheology, and is formulated in the time domain, using matrix-constructions of the analytic solutions for homogenous mantle layers and continuity conditions on displacement, stress and perturbed gravitational potential at each boundary. The equation system is derived from the Lagrangian form of the perturbation equations for mass and momentum conservation, gravitational-potential and constitutive equations. The matrix-system of interface conditions is solved as an eigenvalue-eigenvector problem without the use of propagator matrices. The numerical code reduces to one that solves an

initial-value problem for ordinary differential equations using the method described in (144). Extensions of the method have been explored by (145).

The code employed by (35) uses the same basic form of the perturbation equations, but additionally accounts for material compressibility of the solid Earth, and incorporates ocean loading via solutions to the Sea Level Equation that include the gravitationally-coupled displacement of the ocean floor (146). The effects of rotational feedback, as described in (147), are also included. (73) also incorporates ocean loading, but does so with no iterative solution of the formal Sea Level Equation.

For each model calculation there is a predictive set of quantities:  $u_r(\theta, \varphi, r, t)$  and  $\partial_t \Phi'(\theta, \varphi, r, t)$ , where  $u_r$  is the radial bedrock velocity and  $\partial_t \Phi'$  is the time derivative of the external potential field caused by deformation throughout the Earth, including at the surface,  $r=R_e$ . For both the IJ05\_R2 and W12a model runs the predicted values at present-day ( $t_{pd}$ ) of  $u_r(\theta, \varphi, R_e, t_{pd})$  and  $\partial_t \Phi'(\theta, \varphi, R_e + a', t_{pd})$  may be compared to GPS monitoring of vertical bedrock motions and to spacecraft accelerations at altitude  $a'$ , respectively. The use of such solutions with GRACE data is straightforward: each of the analysis center releases are in terms of spherical harmonic coefficients,  $C_{lmj}$ , and can be directly compared to the expansion coefficients,  $^{GIA}C_{lmj}$ , that are formed from each GIA computation (see (73), equation 8, therein). The W12a model computations have the added advantage that they may be used to compare model predictions with RSL data, and this aids in limiting the Earth structure model space to those which best fit the latter data set (35). This is a fundamental difference in the computations of IJ05\_R2 and (35), and it influences the spatial variability of the GIA-correction and inference of mantle viscosity. However, the continent-wide correction does not seem strongly influenced. There is an additional computational difference that should be of note for future study: the W12a and IJ05\_R2 series assume the end of model loading/unloading to be 0.1 and 1.0 ka, respectively. Both W12a and IJ05\_R2 are ice models that are free from assumptions of Earth rheology.

#### §4.2.2 Model calibration

In calculating the model output,  $u_r(\theta, \varphi, R_e, t_{pd})$ , for a wide host of plausible upper and lower mantle viscosities, and lithospheric thicknesses, we may compare the modelled results to observed GPS station values. Only the highest quality GPS data capable of resolving secular vertical crustal motion were used in the analysis for IJ05\_R2, limiting the number of stations outside the Antarctic Peninsula to 18. (35) compared model results to 35 stations and include stations in the Antarctic Peninsula. Both analyses used trends reported in (34). However, for the purposes of the Ice sheet Mass Balance Inter-comparison Exercise (IMBIE) exercise, the IJ05\_R2 results shown in Fig. S7 use the solutions for vertical displacement rates with no elastic correction. These corrections can only be derived from the ice mass balance trends determined by satellite methods. The spherical harmonic truncation for uplift predictions occurred at degree and order 256. Both analyses assume a melt-water far-field history derived from the northern hemispheric component of ICE-5G.

ICE-5G (39) is the 'standard' ice model recommended in GRACE releases (148). Use of ICE-5G is important in that the loading of the adjacent ocean is consistent with global postglacial sea-level change and it ensures that the low order spherical harmonic field is captured in the predictions. According to tests performed by (133) for IJ05 and ICE-5G,

higher order sea-level loading effects are likely to have a negligible impact on results derived for space-gravimetric and altimetric GIA-corrections.

#### §4.2.3 GRACE correction

As noted above, each well-performing model  $u_r(\theta, \phi, R_e, t_{pd})$  has a unique counterpart:  ${}^{GIA}C_{lmj}$  and those predictions form the sought-after GIA corrections. It is important to point out the level of improvement in such GIA predictions: a new GPS data set, rich in both space and time (34), has been used to constrain or test the ice forward models. These GPS data had previously *not* been used to constrain *any* of the models for GRACE or space altimetry correction.

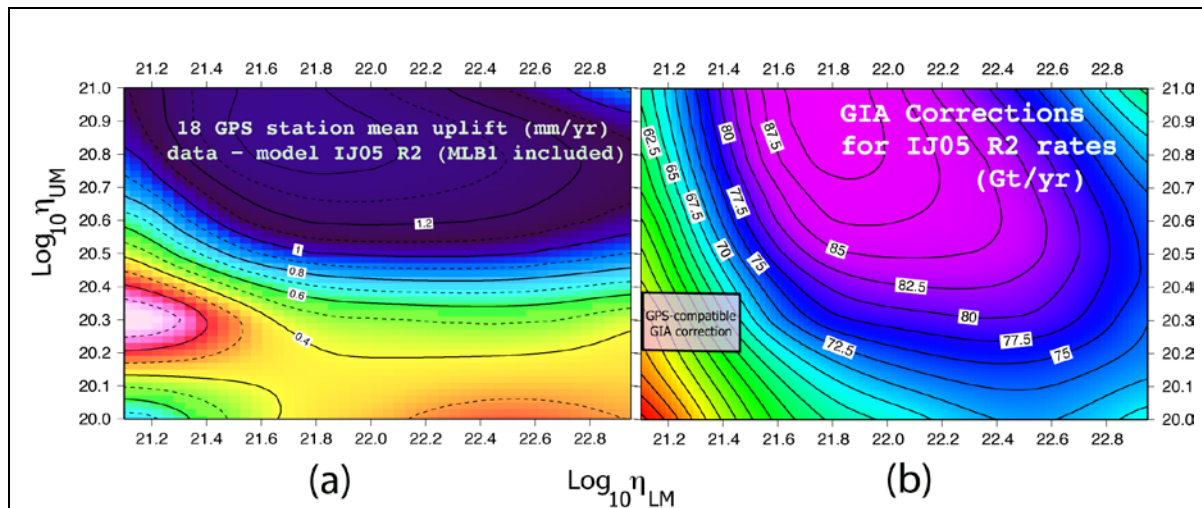


Figure S7. IJ05\_R2 ice model Earth response predictions for lithospheric thickness  $h = 65$  km. Left panel (a) shows absolute mean differences to 18 GPS vertical trends selected from (34). Best performing solutions are shown at the lower left of (a), where contour values are below 0.2 mm/yr. Using the same GIA model runs, corresponding corrections (Gt/yr) are shown in the right panel (b). The values were computed using the averaging kernel technique described in (149), with scale factor of 1.256, no degree 1-terms, truncation at degree and order 60, and Gaussian isotropic filter radius of 300 km.

In the parameter study undertaken for IMBIE, with constraint by GPS vertical motion data (e.g. (34)), we were able to determine a new set of optimum GIA corrections. These corrections are shown as a comparison to the absolute mean uplift (left frame, a) and in Gt/yr mass rate equivalent (right frame, b) in Fig. S7. Use of a Chi-squared comparison for each of the 18 station uplift data leads to the same conclusion: that the GIA correction is robustly confined to the range given in the box on the lower left of (b) in Fig. S7. This bounds the GRACE GIA-correction to between 40-65 Gt/yr.

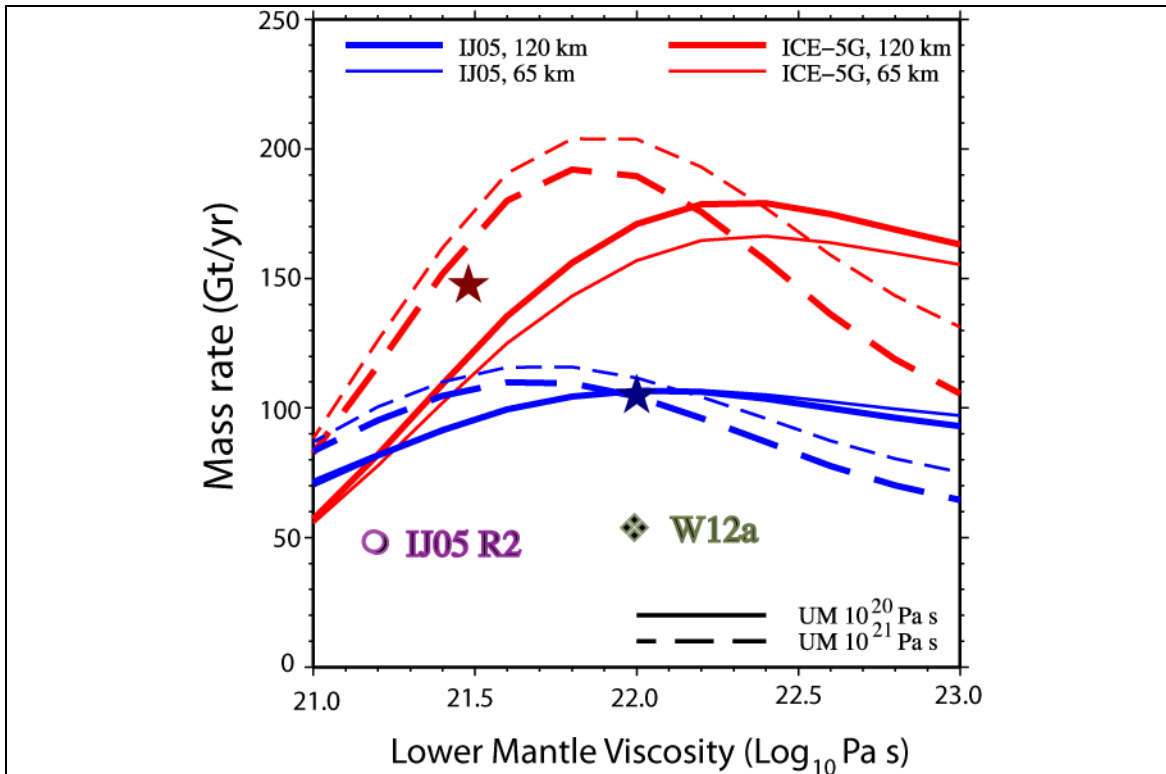


Figure S8. The optimum IJ05\_R2 and W12a model corrections vs. the past IJ05 and ICE-5G corrections employed for GRACE Antarctic ice mass balance analysis. Model GIA calculations of IJ05 and ICE-5G assume two lithospheric thicknesses ( $h = 120, 65$  km) and two upper mantle viscosities;  $\eta_{UM} = 1 \times 10^{20}$  Pa s and  $\eta_{UM} = 1 \times 10^{21}$  Pa s. (See Fig. S6 for the differences in melt history). Error bars for the open circle and diamond are  $\pm 4$  Gt/yr, based upon scatter in the filtering methods that were tested in the course of the IMBIE. The blue star is placed at (41) recommended ‘stiff’ Earth structure model, and the red star, near the structure model advocated by (39) based upon global inversions. The two new optimum models are discussed in the text of this SOM. (Adapted from (32)).

Fig. S8 presents a summary of the two most widely employed model corrections (ICE-5G and IJ05). (32) noted how large these corrections were: about 140-180 Gt/yr and 90-110 Gt/yr, for the two models, respectively. The implied variance is at a level of 150 Gt/yr, clearly a disturbingly large source of GRACE-uncertainty for determining Antarctic ice mass balance. (31) suggested a reduction of the GRACE GIA-correction in the first report of spatially comprehensive GPS vertical trends, without dealing with any model adjustment.

The mass rate correction in Fig. S8 shows that the level of variance is a sensitive function of the lower mantle viscosity parameter (horizontal-axis) for ICE-5G, but less so for IJ05. This can be explained by the differences in size of the two models: ICE-5G is approximately 1.75 times more massive in total continent-to-ocean mass transfer, and therefore, deformation penetrates deeper into the solid earth (also see (102)), well below the 670 km seismic discontinuity that marks the boundary between upper and lower mantle. The ICE-5G model melt-water expulsion is about 2.4 times greater than that in the revised R2 version of the IJ05 model. The later model exhibits even less sensitivity to

lower mantle viscosity than past models. Nonetheless, predictions from the revised model are highly sensitive to upper mantle structure. The GPS data, even with relatively poor spatial sampling, are therefore crucial to further reducing the uncertainty in the GIA correction.

Comparison of the IJ05 and ICE-5G mass rate corrections (at the star-values in Fig. S8) to the optimum IJ05\_R2 (open circle) and W12a (diamond) values reveals that corrections are reduced by about 95-100 Gt/yr, when compared to ICE-5G and 45-50 Gt/yr when compared to IJ05.

It is important to inspect the plan-view maps of the spatial pattern and amplitude of the predicted GIA corrections as a direct comparison to the GRACE trend determined using monthly CSR-RL04 over the 9-year GRACE observing period: 2003-2011. The maps give an indication of how large, and in what regions, the GIA corrections may corrupt interpretation of the GRACE signal. Fig. S9 shows the solved-for trend using least squares fitting to linear, constant off-set, annual, semi-annual, two prominent tidal aliasing amplitudes ( $K_2$ ,  $S_2$ ) and phases in the spherical harmonic coefficient domain. The GRACE time series is 9 years long, so we can include the diurnal  $K_1$  tide that has an aliasing period near 7.7 years (150, 151). However, this is dangerously close to the cycle itself and results here are given with the shorter (2.6 year) periodicity removed. To obtain a ‘GIA-corrected’ map of secular ice mass loss observed by GRACE, the corrections (frames S9 b or c) should simply be subtracted from frame (a).

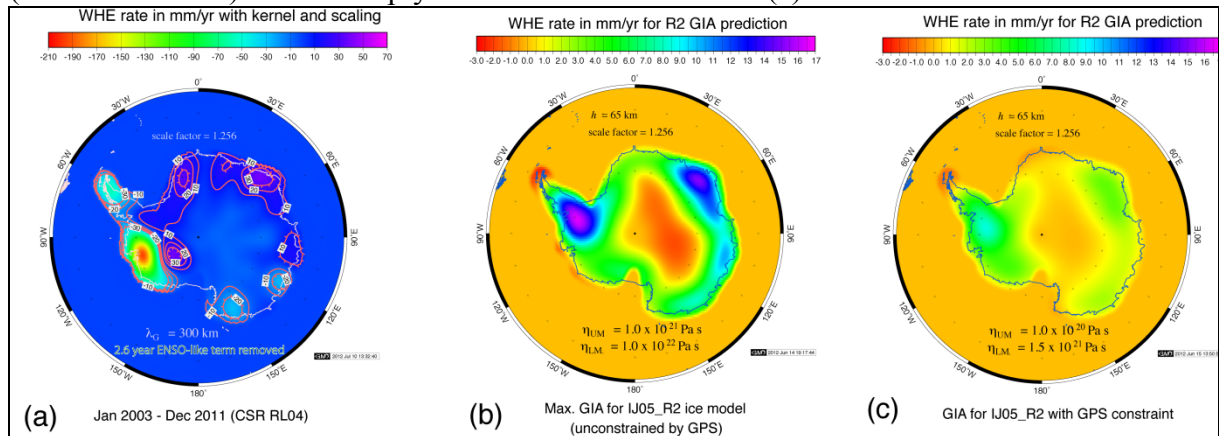
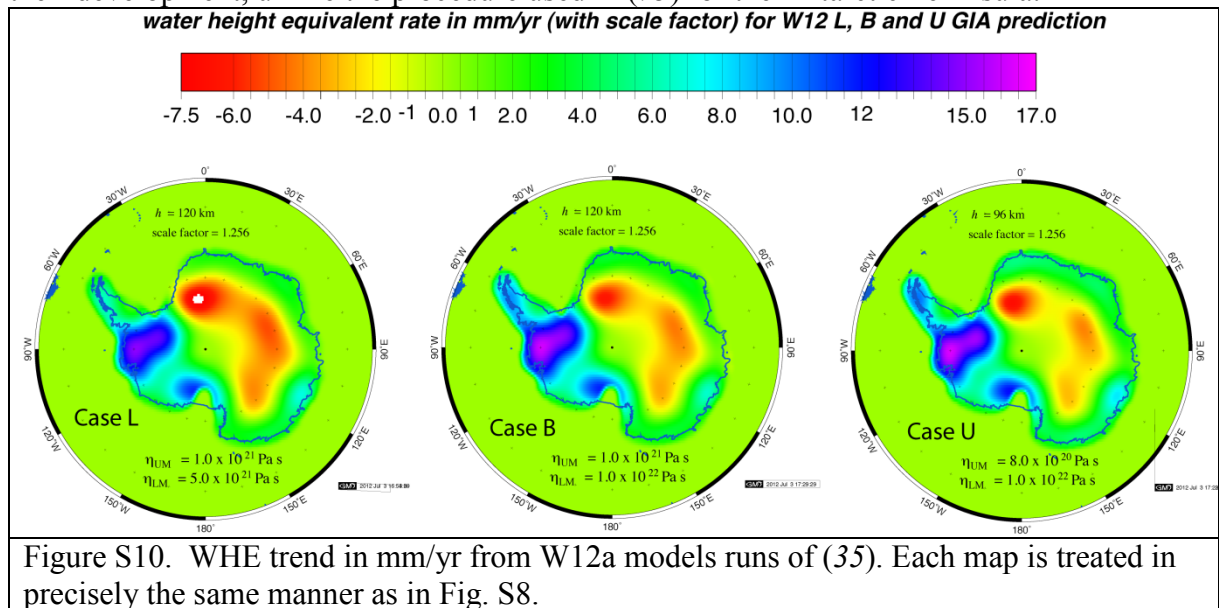


Figure S9. Water-height equivalent (WHE) trend in mm/yr from GRACE time-series (a), and GPS-unconstrained (b) and GPS-well-constrained GIA-trends (c). Here the GRACE data use a kernel and rescaling approach as described by (149) and time-series coefficient spectral analysis as described by (73). Each map has trends that are smoothed with a Gaussian radius,  $\lambda_G = 300$  km. Note the differences in colour scales between (a), and (b) and (c).

The smaller amplitude GPS-constrained (see box in Fig. S7) GIA of IJ05\_R2 (frame S9c) reflects the fact that the new, data-constrained, corrections are less than half the raw uncorrected trend everywhere in East Antarctica, and, more generally, are between 1/10<sup>th</sup> and 1/5<sup>th</sup> the GRACE trend amplitude. In the interior of East Antarctica the GRACE GIA-correction is small and negative ( $\sim -1$  mm/yr), while in West Antarctica the largest GRACE GIA-corrections coincide with the largest model uplift in space, and vary between 3-9 mm/yr water-height equivalent (WHE). These corrective rates are roughly a 1/3<sup>rd</sup> of the peak-amplitudes of the original IJ05 model, which was not constrained by GPS data. In Fig. S10 the WHE rates for the lower (L), ‘best’ (B) and upper (U)

bounding W12a model runs are shown, filtered exactly the same way as in Fig. S9. Here the differences between IJ05\_R2 and W12a are notable, and they reflect the different assumptions that have gone into dealing with the IHD paleo-reconstruction data, and the intermediate step used in W12a where the RSL data sets are used to tune the Earth model. The ‘L’ and ‘U’ W12a solutions are those that produce the smallest and largest positive peak in WHE rate, respectively, and yet satisfy the data constraints employed in the models (to within their errors). W12a run ‘B’ refers to that model run best satisfying all these data. The contrast in amplitude and spatial configuration of the negative depressions of WHE values in central East Antarctica (in red) in Figure S10a-c is important, for here there are few constraints on the models. Finally, it is important to point out that none of the new models reported here incorporated any GRACE data in their development, unlike the procedure used in (73) for the Antarctic Peninsula.



The regional data-assimilating AIS ice models used here, including the M11 model (Fig. S6), have a total volume equivalent to sea-level low-stand at LGM reduced by 10 meters in comparison to ICE-5G. Both ICE-5G and the ANU models are tuned to a value of low-stand at 21 ka of near -123 meters, relative to present-day. While the errors of global LGM low-stand lie roughly between,  $\pm 2$  meters to  $\pm 10$  meters (e.g., (152)), the AIS reduction of 10 meters causes concern over how to close the global mass budget required by the low-stand observations. It remains to be seen how this question will be resolved.

## §5. Radar Altimetry Methods

We use satellite radar altimeter observations to determine changes in the mass of the EAIS and the WAIS, following methods established in previous studies (4,11,15,49,50,52,53,74). We do not present radar altimeter observations of the GrIS or the APIS, because the typical scale of outlet glaciers in these regions is small in comparison to the size of the pulse-limited altimeter footprint, which leads to significantly reduced data volumes in the ice marginal regions. Time-series of surface elevation change are developed at crossing points of the satellite orbit ground tracks using dual cycle crossovers. The elevation data are corrected for the lag of the leading

edge tracker, and for variations in dry atmospheric mass, water vapour, the ionosphere, ocean loading tides and surface scattering. The IJ05\_R2 model is used to correct for the effects of GIA, a correction that is, on average, a small (~7 %) fraction of the observed elevation change. The difference between using this model and the W12a model amounts to ~4 Gt/yr, which is small compared to the total Antarctic mass signal. Time-series of elevation differences derived from the ERS-1, ERS-2, and Envisat satellite radar altimeters are cross-calibrated and merged to form a single time-series spanning the period 1992-2011. The conversion from volume to mass change can be performed using either an external model of fluctuations in the firn layer thickness (e.g. 29, 51) or by using a prescribed model of the density at which elevation changes occur (eg. 4, 52). In the case of radar altimetry, the latter approach is employed because the observations are relatively insensitive to fluctuations in surface mass balance due to penetration of the radar signal into the firn pack and, in consequence, models of firn layer fluctuations are not well correlated with the observed elevation changes. In practise, it has not yet proved possible to separate, in the observed elevation change, annual cycles due to density fluctuations from residual variations due to signal penetration into the firn.

In total, 46.5 million individual satellite radar altimeter elevation measurements are included in this analysis, encompassing 74 and 76 % of the EAIS and WAIS, respectively. The vast majority (92 %) of the un-surveyed region lies south of the latitudinal limit of the radar altimeter coverage, where little or no signal of mass change is believed to occur. The remainder is located in regions of steep terrain, including the Transantarctic Mountains and the ice sheet margin. Although there are large signals of mass loss in some coastal regions of Antarctica, our survey extends to, on average, 8.8 km of the ice sheet margin, and even closer (2-4 km) in the WAIS, where the majority of mass losses are known to occur. In a previous study (52), we estimated the potential scale of mass changes in these two main areas of omission. Based on a consideration of the mass changes in adjacent areas, we estimated the mass balance of the coastal and central ice sheet omission regions to be -10 and +7 Gt yr<sup>-1</sup>, respectively, signals that are small in comparison to both the estimated ice sheet mass imbalance and its uncertainty, and also offset one another. In this study, we do not make such an estimate, because the coastal region - the area of greatest concern - includes considerably more data due to the use of additional reference cycles, and the improved tracking of the Envisat radar altimeter. Instead, we scale the observed signal of mass imbalance within each glaciological drainage basin in proportion to the unobserved area, to provide an estimate of the total mass imbalance of the EAIS and WAIS that is consistent with approaches employed elsewhere.

To estimate the uncertainty of the ice sheet mass trends, we treat the estimated variability of snowfall and the elevation trend variability as equivalent sources of uncertainty. In practise, this leads to estimated uncertainties that are larger for small regions, because the uncertainty of snow accumulation and the variance of elevation trends are proportionally greater. In keeping with other partial surveys of ice sheet mass balance (e.g. (14,18,55,57)), and with our own previous studies (e.g. (52)), we scale the estimated uncertainty of mass imbalance within each glaciological drainage basin in proportion to the unobserved area, to provide an estimate of the uncertainty associated with the mass imbalance in the regions of omission.

A complete explanation of the radar altimeter data processing scheme, and the geophysical corrections applied, can be found in previous studies, and the references therein (e.g. (11,49,50,52,74)). Here, we provide a detailed discussion of three key aspects of this processing scheme that are of particular relevance to the present study. In section S5.1, we describe the method employed to cross-calibrate the various satellite altimeter records. In section S5.2, we describe the model used to estimate the density of ice sheet elevation fluctuations. In section S5.3, we describe the method employed to estimate the ice sheet mass balance uncertainty associated with uncertainties in SMB (which we do not model).

### §5.1 Cross Calibration of Satellite Sensors

In order to combine elevation change measurements acquired by multiple satellite sensors, it is necessary to identify the relationship between the systematic errors of the satellites, so as to account for any inter-campaign bias inherent in the complete elevation time-series. We achieve this cross-calibration by calculating inter-satellite elevation biases occurring during periods of mission overlap. Specifically, we assume that the systematic error in the satellite measurement is constant in time, but may be spatially dependent. Taking Envisat as our reference satellite, we estimate the relative bias of ERS-1 and ERS-2 at each grid cell, according to the availability of coincident data at that grid cell. If the time-series of the two satellites overlap, then the bias is set to the mean difference between the overlapping data. If there is no overlapping data, then we fit a model (functional form  $a + b \cdot t + c \cdot \sin(2\pi t + d)$ ,  $t$  denotes time) to the data acquired by each sensor during the overlap period, and estimate the bias as the mean difference between the modelled elevation changes. Where there is no valid data during the overlap period we make no estimate of inter-campaign bias. The uncertainty associated with the cross-calibration of the various satellite altimeter sensors is included in our estimate of the overall uncertainty of the altimeter-derived rates of ice sheet mass balance.

### §5.2 Density model

For an ice column, the thickness rate equals the mass imbalance divided by the density at which the thickness change occurs. However, because the near surface is composed of snow densifying under its own weight, an accumulation fluctuation will appear in the thickness rate with an effective density that lies between that of snow and ice, and that depends on the time scale of the fluctuation. Estimating the density of observed ice sheet elevation fluctuations is an important step in the process of estimating ice sheet mass imbalance, and different approaches to the conversion have been taken. In the case of satellite radar altimetry, the conversion to mass has been performed using a prescribed density model, and by allowing for temporal fluctuations in snowfall as a separate term in the mass imbalance uncertainty (52) (see section S5.3).

In the ice interior, decadal and century-scale fluctuations will occur with densities close to those of snow and ice, respectively (153). Here, we use this two-scale approximation, updated to account for an improved understanding of the locus of ice dynamical imbalance. Although elevation signals associated with fluctuations in surface mass balance and ice dynamical imbalance may offset one another, we account for this by increasing the uncertainty of the overall mass balance due to observed variations in surface mass balance (see Section 5.3). We assign firn and ice densities of 400 and 900  $\text{kg m}^{-3}$ , respectively, and we develop an objective classification to discriminate between

elevation fluctuations occurring at each density. The aim of this classification is to reproduce the key signals of ice mass imbalance that are known to be driving sustained patterns of elevation change across the AIS. In West Antarctica, we assume that regions experiencing sustained and significant rates of elevation change of magnitude exceeding an empirically-determined cut-off rate are dynamic in origin, and are therefore occurring at the density of ice. Elsewhere, including the remaining regions of West Antarctica and all of East Antarctica, we assume that elevation changes are caused by surface mass balance fluctuations alone, and we therefore assigned a density of snow to these signals in our mass loss calculation.

The spatial distribution and sensitivity of the density model are illustrated in Fig. S11. An absolute cut-off elevation rate of  $7.5 \text{ cm yr}^{-1}$  was chosen as a value that best identifies the areas of known dynamical imbalance, as revealed using a wide range of geophysical techniques (e.g. (11,77,154)). These major signals of ice dynamical imbalance are marginal ice sheet thinning along the Amundsen and Bellingshausen Seas, and ice sheet thickening inland of the Siple Coast. Although the density model performs well in isolating these signals, in practise the resulting estimated WAIS mass imbalance is only weakly sensitive to the cut-off rate, and the range of potential mass imbalance solutions falls well within the uncertainty range determined from systematic errors and estimated fluctuations in SMB (see section S5.3).

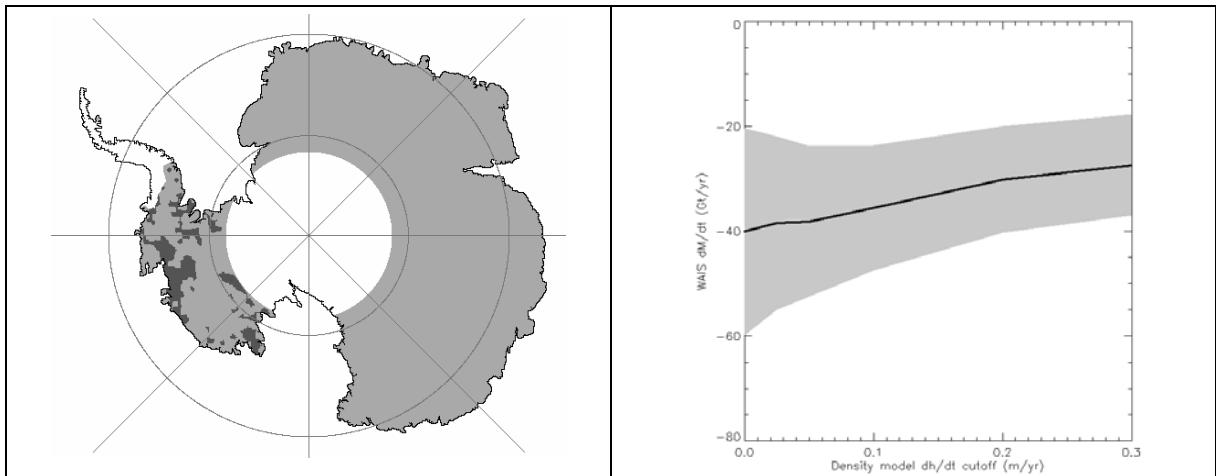


Figure S11. (left) Discrimination between elevation fluctuations occurring at the density of ice (dark grey) and snow (light grey) as determined using a model of density based on an absolute elevation rate cut-off of  $7.5 \text{ cm yr}^{-1}$ . White areas indicate regions outside the altimeter region of coverage. (right) Sensitivity of observed WAIS mass imbalance as a function of the cut-off rate used to define the density model (black line), plus estimated mass imbalance uncertainty (grey). Density model cutoffs equal to zero and one correspond to the cases where the observed elevation fluctuations are assumed to all occur at the density of ice and snow, respectively. In practise, only a narrow range of cut-off rates (between  $0.5$  and  $0.10 \text{ m yr}^{-1}$ ) lead to density models that identify the known signals of ice dynamical imbalance.

### §5.3 Surface Mass Balance

Surface elevation changes occur when the accumulation rate departs from the long-term mean. Over the period of the satellite survey, surface mass balance fluctuations may therefore contribute to estimates of secular mass trends. We account for this effect by following the approach of our previous studies (e.g. (49)). We do not attempt to model these variations, because the elevation and modelled accumulation fluctuations are not always well matched or in phase (52). Possible reasons for this mismatch include residual variations in the radar altimeter observations due to signal penetration into the firn, and uncertainties in model predictions of SMB temporal variability. Instead, we treat the accumulation fluctuations as an additional source of uncertainty in our estimates of mass trends, and we estimate their magnitude from ice core records and model estimates of regional accumulation rates (49).

According to an analysis of in-situ observations (49), the 5-year variability of Antarctic accumulation fluctuations falls in the range 3 to 19 % of the long-term mean accumulation rate (MAR); published data include values of 3, 11, 14, 15, 17, and 19 %, respectively (155-160). We use these observed fluctuations, which are three to four times larger than the 5-year variability of snow accumulation rates derived from regional climate models (< 5 %, according to the analysis presented in §3), as the basis for estimating the uncertainty in ice sheet mass balance associated with un-modelled SMB. Taking a conservative value from the variability of ice core records, we estimate that the 5-year variability in snow accumulation ( $\sigma_{SMB5}$ ) is 15 % of the MAR, and we assume that the temporal variability of the associated elevation fluctuation is therefore

$\sim \sigma_{SMB5} MAR / \rho_{SNOW} \left( \frac{\sqrt{5}}{\sqrt{N}} \right)$  where  $\rho_{SNOW}$  is the density of snow and  $N$  is the period of the fluctuation, in years. Over a region that is large in comparison with the correlation scale, the spatial variability of snow accumulation fluctuations is  $\sim \sigma_{SMB5} \sqrt{\overline{MAR^2}} / \rho_{SNOW} \left( \frac{\sqrt{5}}{\sqrt{N}} \right)$ , where  $\overline{MAR^2}$  is the area average of  $MAR^2$ . The temporal variability of an area average of elevation rate is  $\sim \sigma_{SMB5} \sqrt{\overline{MAR^2} / n} / \rho_{SNOW} \left( \frac{\sqrt{5}}{\sqrt{N}} \right)$ , where  $n$  is the effective number of independent values of  $MAR$  within the region, and we take  $n \sim A / 200^2 \pi$ , where  $A$  is the area in square kilometres and if  $n < 1$  we set it equal to unity. Finally, in this study, we use a regional atmospheric climate model (26) to estimate the MAR within areas of interest, including individual glacier drainage basins, drainage sectors, and ice sheet regions. Using this approach, the 19-year variability of elevation changes associated with surface mass balance fluctuations is estimated to be 0.41 and 2.26 cm yr<sup>-1</sup> for the EAIS and WAIS, respectively.

## § 6. Laser Altimetry Methods

The analysis of ICESat data was performed independently by four different groups: Louise Sørensen and René Forsberg (SF) at the Technical University of Denmark, Hamish Pritchard (HP) at the British Antarctic Survey, Donghui Yi and Jay Zwally (YZ) at NASA Goddard Space Flight Center, and Benjamin Smith (BS) at the University of Washington. Each group used a variant of along-track processing to derive elevation-change rates from the ICESat data. For all of the groups, along-track processing of ICESat data gave a set of point estimates of the elevation rate, located along the satellite

ground tracks. Each group interpolated between these point measurements to form a regular grid of elevation-rate estimates, and integrated these grids over the sectors to give volume-change estimates. The details of each group's processing are described below. The conversion from volume to mass change can be performed using either an external model of fluctuations in the firn layer thickness (e.g. 29, 51) or by using a prescribed model of the density at which elevation changes occur (e.g. 4, 52). In the case of laser altimetry, the former approach is employed because the observations are highly sensitive to fluctuations in surface mass balance as the laser signal is scattered from the firn/air interface. Because of this sensitivity, it is important to make an explicit correction for the effects of fluctuations in surface mass balance.

### § 6.1 GIA correction

For Antarctica, all groups' elevation-change rates were corrected for post-glacial rebound using the W12a and IJ05\_R2 GIA models. The difference between these models for the final result in Antarctica comes to around 4 Gt/yr, which is small compared to the total Antarctic mass signal, so only the W12a result is included in the final tally. For Greenland, SF used ICE-5G, while YZ used a combination of three models (110), but since in each case the correction was smaller than 1 Gt/yr, the difference between these and the preferred IMBIE models is not important.

### § 6.2 Bias correction

SF, HP, and BS each corrected the elevation data for an apparent bias in the ICESat elevations obtained by comparing ICESat's elevations with sea level at latitudes equatorward of 66 degrees, using only data for which no receiver saturation was detected (i.e. the saturation correction was zero). The corrections were updated between releases of the ICESat data (e.g. 32), but were calculated by the same group using similar techniques (Tim Urban, personal communication). The corrections applied by HP to ICESat release 428 data over Antarctica differ slightly from those calculated for the more recent releases (431 and 633) used by SF and BS respectively. Table S5 gives the two sets of corrections that the groups subtracted from the surface-elevation values. Subtracting this correction from the data yields elevations relative to sea level, but sea level was rising during this period by approximately 0.3 cm/yr, so each group then added 0.3 cm/yr to their elevation rates, giving an estimate of the volume change of the ice sheet itself. Including the correction for sea-level change, the trend in the correction is approximately 0.65 cm/yr, equivalent to around 73 Gt/yr for Antarctica.

The groups were not unanimous in their judgment that such a bias represents a valid correction to the data; YZ felt otherwise, and did not apply it. Discussions within the ICESat community have resulted in a statement indicating that residual biases exist in the data but the magnitude of this correction is not well known ([http://nsidc.org/data/icesat/pdf/inter-campaign\\_bias\\_notice\\_v1.pdf](http://nsidc.org/data/icesat/pdf/inter-campaign_bias_notice_v1.pdf)). The error in the composite mass-change rate is approximately equal to the magnitude difference between the corrected and uncorrected volume-change rates, so treating the disagreement between the groups over this issue as an error results in approximately 40% larger errors in the composite elevation-change rate.

Table S5. Bias estimates for ICESat elevations relative to ocean-surface elevation for release 633 (T. Urban, personal communication) and 428 data (161).

Campaign	Release 633 bias (cm)	RMS (cm)	Release 428 bias (cm)	RMS (cm)
2a	-6.8	1.4	-7.4	1
2b	-5.2	1.4	-5.7	1
2c	0.6	5.3	-2.3	2
3a	-3.8	0.9	-2.2	1
3b	-3.4	1.1	-3.3	1
3c	-0.1	1.5	-0.2	1
3d	-0.3	0.9	0.3	1
3e	-0.2	0.7	-0.1	1
3f	-0.9	1.1	-1.2	1
3g	1.3	0.7	1.4	1
3h	0.8	0.9	0.1	1
3i	-0.5	0.9	0.3	1
3j	-1.4	1.3	-1.7	1
3k	-0.4	1.4	0.4	2
2d	1.6	1.8		
2e	5.2	4.4		
2f	-1.1	1.3		

### § 6.3 Volume-to-mass conversion

To convert these volume-change estimates to mass-change estimates, the groups used firn-column models, forced either by temperature and accumulation estimates based on atmospheric reanalysis modelling (29) or on remotely-sensed surface temperature estimates and accumulation variations as a function of temperature (48,51).

For Antarctica, SF, HP, and BS used a reanalysis-driven firn column model. Six-hourly estimates of snowfall, sublimation, melt, rain and surface temperature derived from RACMO2 were used to drive a firn densification model over the AIS (29,161). This one-dimensional model calculates spatial and temporal variations in firn layer temperature, depth and mass at high vertical and horizontal resolution (~5 cm and ~27 km, respectively), allowing for melt-water penetration, retention, refreezing and delayed runoff. The primary application of these data is to adjust satellite laser altimeter observations for the effects of short-term fluctuations in firn thickness. The linear trend between the beginning and end of the period has been subtracted from the data for each grid cell, so the measurements give a detrended anomaly to the longer-term firn-column height variation. BS subtracted the firn-column thickness estimate from each of the surface height data before calculating the elevation rates, HP and SF subtracted the mean rate of firn-column-thickness change from the elevation-rate trends for each ice-sheet sector. Subtracting the firn-thickness anomaly in this way gives estimates of the elevation rate for a constant accumulation rate equivalent to the 1979-2011 mean, at the density of

ice. To produce mass-rate estimates comparable to GRACE results, each group multiplied their volume-change rates by the density of ice, and added RACMO mass-balance anomaly rates to obtain a mass-balance rate for each sector. The errors in the firn-thickness change estimates are based on spatial bias errors provided with the model, and a worst-case estimate of the temporal variation error derived by assuming that the error was equal to the total annual mass-balance variability between 1979 and 2011 for each region, and assuming that the measured mass-balance variation came from an average of five independent samples from this distribution. The errors are then a quadratic sum of the spatial and temporal error estimates.

For Greenland, SF used a novel firn-compaction model (109) driven by the HIRHAM5 regional climate model (162).

For both Antarctica and Greenland, YZ used a firn model with a physical formulation similar to that used by the other groups, but instead of using reanalysis data, they provided accumulation and temperature estimates to their model based on AVHRR (Advanced Very High Resolution Radiometer) surface-temperature estimates, estimating the precipitation anomaly based on an assumed correlation between temperature anomalies and precipitation anomalies (51). Their formulation allows separation of compaction changes driven by accumulation and temperature variation, so they did not perform separate steps of subtracting and adding anomalies as did the other groups.

#### § 6.4 BS volume-change estimates

BS produced mass-balance estimates for WAIS and EAIS. He used release 633 ICESat data, obtained from the National Snow and Ice Data Center. To remove distorted returns and returns excessively affected by cloud cover, he applied a set of editing criteria that remove around 20% of returns from each campaign based on the parameters describing the shape and amplitude of the returned surface pulse: returns were accepted only if the apparent surface reflectance was greater than a specified minimum, and if the shape of the returned pulse matched a Gaussian fit to within a specified maximum (Table S6). BS calculated elevation rates for short (340-meter) segments of the repeat track using a multiple-regression model that solves for the least-squares estimate of the surface slope and elevation-change rate (163). For each segment, this yielded a slope estimate, an elevation-rate estimate, an error estimate, and an RMS misfit between the regression and the data. He rejected elevation-rate estimates for which:

- fewer than five repeat measurements were available
- the RMS misfit was greater than 10 m
- the surface slope estimate was larger than 5 degrees
- the elevation error rate estimate was greater than 2 m/yr
- the available data did not span the time period between June 1 2004 and September 1 2007.

He then picked a representative subsample of these estimates by selecting the estimate with the median elevation rate for each 10x10 km grid cell on the grounded ice in Antarctica, and interpolated between these median points to a 1-km grid using an inverse-distance-weighting scheme, then smoothed and subsampled this 1-km grid to the 5-km IMBIE reference grid. His reported elevation-rate values are calculated based on the IMBIE grid.

Table S6. Editing criteria for ICESat surface returns used in BS elevation-rate estimates.

Campaign	Minimum uncorrected reflectance	Maximum fit variance (V)
2a	0.0375	0.0375
2b	0.0125	0.03
2c	0.0125	0.02
3a	0.0375	0.04
3b	0.0375	0.038
3c	0.025	0.0425
3d	0.025	0.0225
3e	0.025	0.035
3f	0.025	0.0275
3g	0.025	0.025
3h	0.05	0.03
3i	0.05	0.0275
3j	0.05	0.03
3k	0.025	0.025
2d	0.025	0.02
2e	0.1	0.02
2f	0.075	0.02

### § 6.5 HP volume-change estimates

HP produced a mass-balance estimate for WAIS. He used ICESat GLA12 Release-428 data corrected for saturation and intercampaing bias (161), excluded cloud-affected data using waveform parameters (163) and calculated along-track elevation rate using an established method that employs linear interpolation between parallel, repeated satellite passes (77). He filtered out elevation rates that differed by more than 0.75 times the interquartile range from the median over a radius of 25 km from each point and produced a smoothed, 5 km grid of the mean (77). He interpolated a continuous elevation-change field from these data using inverse distance weighting, and integrated this to calculate  $dV/dt$  estimates.

### § 6.6 SF volume-change estimates

SF produced mass-rate estimates for all four major ice-sheet divisions. They used release 431 ICESat data, and followed methods described in (109). They selected data points using a fixed maximum on the waveform fitting fit parameter (IceSvar) of 0.04 V, and rejected waveforms with multiple peaks. They fitted the ICESat data using the same multiple-regression technique as BS (163), but included sinusoidal terms to take into account seasonal elevation variations. They used a collocation algorithm to map the data to the IMBIE grid, using weights based on the formal errors on the  $dH/dt$  estimates and a suite of correlation lengths determined from the data, where the weights on the  $dH/dt$

point estimates for each grid point decreased with the distance between the  $dH/dt$  point and the grid point and with the variance of the  $dH/dt$  estimate. They derived volume-change error estimates from the fit formal errors and from the range of gridded  $dV/dt$  estimates obtained using different correlation lengths.

### § 6.7 YZ volume-change estimates

Like SF, YZ produced mass-rate estimates for all four divisions. They used release 633 data for Antarctica, and release 428 data for Greenland. They calculated elevation rates on 1-km segments along track, using a quadratic surface-height variation in the along-track direction to account for local surface-slope variability when adequate data were available, otherwise using a linear fit (110). For each 50x50 km subset of the ice sheet they calculated gridded elevation rates using ordinary kriging, and calculated regional averages from the 50-km cell averages after weighting each cell by the fraction of its area falling within the ice sheet. Antarctic volume rates are corrected for GIA using W12a Greenland rates by a weighted average of three models. Although the Greenland correction did not use one of the preferred IMBIE models, the magnitude of the correction ( $\sim 1$  Gt/yr) is small compared to model errors. YZ corrected all Greenland (release 431) data for estimated bias changes by subtracting an estimate of Arctic-ocean freeboard (110), but made no correction to the Antarctic (release 633) data. Their supplied error estimates include formal errors in  $dV/dt$ , and estimates of the contributions of GIA and firn compaction that are based on a fraction of the magnitude of these signals, as described in (110).

## § 6.8 Results

### § 6.8.1 Volume-change estimates

Table S7 gives the volume-change estimates for the four groups for Antarctica and Greenland. These rates represent the most basic interpretation of the data, with no corrections applied for firn or mass-balance variability. Despite this, there is a large spread in the volume-rate estimates, particularly for West Antarctica, which is not well reflected in the error estimates. With the exception of that from SF, the error estimates represent formal errors on the  $dH/dt$  solution integrated spatially, and thus do not include a realistic assessment of the error due to poor sampling of spatial variations in  $dH/dt$ . Likewise, different data-editing strategies between the groups produce different spatial coverage of measurements, which are not adequately represented by the formal errors. Last, there are important differences between the techniques employed by the different groups, two of which might have generated large differences in rates obtained: First, YZ did not apply a bias correction used by the other three groups and HP used an earlier version of the bias correction than that used by SF and BS. Second, HP used a triangulation approach to compare repeat tracks, which is different from the regression approach employed by the other three groups. YZ's choice should result in more positive elevation rates, as is reflected in their totals, but the expected effect of HP's choice of processing is not easily understood, although a point-for-point comparison of WAIS elevation rates with those calculated by BS using identical data showed only small systematic differences. We have chosen not to include the spread between methods in our final error estimate, in part because there is no clear way to understand the expected distribution of this error, but we note that the spread between volume-change estimates is

comparable to the final error once the uncertainty in firn and mass-balance corrections are included. For this reason, including the standard deviation in the volume-change estimates ( $\sim 13$  Gt/year for EAIS,  $\sim 17$  Gt/yr for WAIS) as a sampling error in the mass-change estimates would increase the total mass-change error by only 2-3 Gt/yr in each case.

Table S7. Volume-change rate estimates (in $\text{km}^3/\text{yr}$ ) based on spatial integrals of interpolated ICESat elevation rates. YZ do not provide a volume-change estimate for Greenland, but provide a $dM/dt$ estimate.					
Contributor	EAIS	WAIS	APIS	AIS	GrIS
SF	$78 \pm 15$	$-29 \pm 8$	$-29 \pm 15$	$20 \pm 23$	$-189 \pm 20$
HP		$-7 \pm 8$			
BS	$63 \pm 27$	$-50 \pm 6$			
YZ	$94 \pm 12$	$-15 \pm 3$	$-27 \pm 3$	$52 \pm 12$	
Mean	$78 \pm 19$	$-25 \pm 7$	$-28 \pm 11$		$-189 \pm 20$
Spread	31	43	2		

### § 6.8.2 Mass-change estimates

Table S8 gives the mass-change estimates based on the volume-change estimates and the volume-to-mass conversions. Mass-change error estimates for each group were calculated as the quadratic sum of each group's volume-change estimate and the estimated error in the compaction and mass-anomaly corrections obtained from the RACMO2 model.

Table S8. Mass-rate estimates based on volume-change estimates, firn-model-change estimates, and mass-balance change estimates.					
Contributor	EAIS	WAIS	APIS	AIS	GrIS
SF	$118 \pm 56$	$-79 \pm 39$	$-33 \pm 21$	$6 \pm 72$	$-197 \pm 23$
HP		$-52 \pm 39$			
BS	$123 \pm 60$	$-95 \pm 39$			
YZ	$86 \pm 55$	$-13 \pm 39$	$-24 \pm 15$	$49 \pm 69$	$-185 \pm 8$
Mean	$109 \pm 57$	$-60 \pm 39$	$-28 \pm 18$	$21 \pm 71$	$-186 \pm 24$
Spread	36	82	9	44	12

The different solutions for this calculation introduce additional spread between the estimates, but the error estimates also increase. Nonetheless, the error estimates for the different techniques are not sufficient to encompass the spread between them, which suggests that the error estimates for laser altimetry carried out in this way are, broadly speaking, too small.

## § 7. IOM Methods

In this section, we provide details on the IOM calculations for Greenland and Antarctica. In the IOM method, total mass balance for each basin is calculated as the difference between the total surface mass balance within the drainage basin minus ice discharge at the exit flux gate of the basin, hence mass balance is positive if the mass input (surface mass balance) exceeds the mass output (ice discharge), and vice versa.

The drainage basins, surface mass balance data and uncertainties are discussed in other sections. Ice discharge is calculated across each flux gate by combining ice thickness and ice velocity data. Here, we describe the flux gates, ice thickness data and ice velocity data employed in our calculations. Results from neighbouring basins are combined together to provide estimates of the total mass balance for the four ice sheet regions discussed in this article (Tables S9 and S10).

### § 7.1. Flux gates

In Antarctica, ice flux gates are located at the grounding line, which is where the ice detaches from the bed and becomes afloat in the ocean. This transition boundary is mapped with a horizontal precision better than 100m using differential satellite radar interferometry (DInSAR) over the vast majority of the continent (*164*). For tidewater glaciers or places where ice does not form a floating section, the grounding line coincides with the ice front position, which is extracted from a digital mosaic of Antarctica using MODIS data (*165*). In Greenland, the flux gates are located upstream of the grounding line along flight lines where ice thickness was measured using airborne radio echo sounding (*166,167*).

### § 7.2. Ice thickness data

In Greenland, we use ice thickness data from radio echo sounding collected by NASA's Mission Operation IceBridge (OIB) and earlier airborne missions flown by NASA (*166*). In Antarctica, we use OIB data (*167, 168*), BEDMAP data (*169*) and estimates of ice thickness from altimetry assuming hydrostatic equilibrium of ice (*170*). Ice thickness is known with a precision of 10 m from radio echo sounding and 80 m from hydrostatic equilibrium (*55*).

### § 7.3. Ice velocity data

Ice velocity is measured using satellite radar interferometry (*63,85,171*) and effectively corresponds to the velocity of the ice surface assuming surface parallel flow. We make no correction to translate surface velocity into a depth-averaged velocity because on fast moving glaciers, i.e. speed > 50-100 m/yr, ice speed is almost entirely due to basal sliding. The error is less than 1 percent and is compensated for by the fact that in Greenland most of our velocity measurements are from the winter season, where ice speed is on average 2 percent slower than the annual average speed (*18*). In Antarctica, seasonal variations in speed are negligible. Ice velocity measured with InSAR uses data collected 24 to 46 days apart, and hence corresponds to a monthly-time-scale average with no tidal signal or hourly fluctuations in speed (e.g. *63*).

#### § 7.4. Ice discharge

In Antarctica, ice discharge is calculated from ice velocity and ice thickness in all areas for which ice thickness is known (Table S9). In areas where ice thickness is not known, ice discharge is assumed to be equal to the total surface mass balance of the basin averaged for the years 1979-2010, i.e. these areas are assumed to contribute zero mass gain for the period 1979-2010 and their ice discharge is assumed to be constant during the entire time period.

In Greenland, we use the same procedure as in (18) to deduce grounding line ice discharge from the mass discharge at the flux gates (Table S10). First, we calculate a reference grounding line ice discharge, for a reference year 1996 or 2000, by correcting the mass discharge on that reference year at the flux gate for the average surface mass balance of the glacier for the years 1961-1990 in the area between the flux gate and the grounding line. On subsequent years, the grounding ice discharge is deduced from the reference ice discharge by correcting for changes in glacier speed (via a percentage) and changes in glacier thickness at the grounding line (via a percentage). The change in glacier speed is calculated as a percentage change in ice speed at the glacier front with respect to the reference year.

Changes in glacier thickness are deduced from multi-date altimetry measurements of the ice surface and are expressed as a percentage change in glacier thickness at the ice front (56). The change in glacier thickness is only significant for glaciers that are thinning rapidly, i.e. at rates > 10 m/yr. For Greenland glaciers and basins with no thickness data (Table S10), we assume that ice discharge is constant and equal to the average surface mass balance for (the balance) years 1961-1990. Estimates of ice discharge that are available at relatively sparse time intervals, when ice thickness or velocity data are updated, are linearly interpolated to provide a continuous dataset.

Table S9. List of glacier names in each region of Antarctica. Gl. = glacier; I.S. = ice stream. In some regions, names were chosen based on a coastline, a major glacier, hills or mountains, but the names are non official. Area in square kilometre lists the size of each drainage basin. The table indicates the year of availability of ice surface observations from 1992-2011 (yellow colour if data is available, no colour otherwise) and the source of the ice thickness data: 1) OIB or BEDMAP data; 2) (170) ice shelf thickness map; or 3) no ice thickness available, in which case ice discharge is equal to the average surface mass balance for the years 1979-2011. See additional Excel Spreadsheet: Tables\_S1\_S3\_S9\_S10.

Table S10. List of glacier names in each region of Greenland. Gl. = glacier; I.S. = ice stream. In some regions, names were chosen based on a coastline, a major glacier, hills or mountains, but the names are non official. Area in square kilometre lists the size of each drainage basin. The table indicates the year of availability of ice surface observations from 1992-2011 (yellow colour if data is available, no colour otherwise) and the source of the ice thickness data: 1) OIB or 2) no thickness available, in which case ice discharge is equal to the average surface mass balance for the years 1961-1990. See additional Excel Spreadsheet: Tables\_S1\_S3\_S9\_S10.

## § 8 GRACE Methods

The GRACE estimates given in the main text were computed from results provided by six separate groups: Valentina Barletta and Rene Forsberg (BF) from the National Space Institute at the Technical University of Denmark; Martin Horwath (H) from Technische Universitaet Munchen; Scott Luthcke (L) from Goddard Space Flight Center; Ernst Schrama (S) from the Delft University of Technology; Isabella Velicogna (V) from the University of California at Irvine; and John Wahr (W) from the University of Colorado. Each group provided monthly time series, apart from L who provided 10-day time series, as well as secular trend values with uncertainties, for each of the five regions (GrIS, AIS, WAIS, EAIS, APIS). In each case, trends were provided for two time spans: Jan, 03 – Dec, 10, and Oct, 03 – Dec, 08. For GrIS and AIS, results were also provided for Jan, 05 – Dec, 10. For each region, the final GRACE time series shown in the main text was computed as the arithmetic average of the 6 individual time series. The final GRACE trends were computed as the arithmetic average of the six individual trends, and the uncertainty interval for each trend was computed as the arithmetic average of the six uncertainty intervals.

Each group computed their time series values, as well as their trends and uncertainties, in their own way. Starting points for each group's approach can be found in (172,173) for BF; (105) for H; (68,72) for L; (84) for S; and (76,82) for V and for W. Some groups (BF, L, S) used a mascon approach, while some (H, V, W) used averaging kernels. Most groups used the Release-4 spherical harmonic gravity coefficients produced by the Center for Space Research (CSR) at the University of Texas, although L used his own independent analysis of GRACE Level-1 data. The groups using CSR fields modified the standard Release-4 fields by replacing the CSR/GFZ/JPL Release-4 ocean model correction, with the improved ocean model correction developed for Release-5. L used the Release-4 ocean model correction. BF, H, S, V, and W replaced the CSR  $C_{20}$  coefficient with  $C_{20}$  coefficients deduced from satellite laser ranging. L's analysis method, which involves fitting mascon amplitudes directly to Level-1 GRACE data, does not explicitly generate spherical harmonic coefficients, and so the issue of whether to replace  $C_{20}$  coefficients does not arise. All groups augmented their results by including contributions from degree-one coefficients provided by Sean Swenson. Those coefficients are used to translate the coordinate system so that its origin is at the geometric center of the Earth's surface.

The GRACE estimates can be contaminated by gravity signals unrelated to the present-day mass balance of the ice sheets and each GRACE group either corrected for, or evaluated the uncertainties from some or all of those signals. Contamination can be separated into (1) signals from regions above (the atmosphere) or below (the solid Earth) the ice sheet for which probably the only significant solid Earth contamination comes from GIA and (2) signals originating from locations on the Earth's surface external to the ice sheets. Sources of contamination from (2) include the storage of liquid water and snow on land outside the ice sheets, and ocean signals not already included in the standard GRACE ocean model correction. Mass loss from the small ice caps directly peripheral to the ice sheets was not removed, but was included as part of the GRACE ice sheet estimates. Atmospheric corrections are made during Level-1 processing using atmospheric fields. There are errors in those atmospheric fields that could be contributing

to the notable short-period scatter in the AIS and EAIS time series. But, when the atmospheric corrections are added back to the GRACE fields and the results are averaged over entire ice sheets, there is little impact on the derived trends. So it is unlikely that errors in those corrections would have a significant impact on the estimated ice-sheet-wide trends, either.

The importance of contamination from signals on the Earth's surface external to the ice sheets, depends on the analysis method. Groups that deemed it necessary to correct for external land water/snow contamination, applied corrections based on the GLDAS/Noah land surface model (174). For the ocean, the principal ocean signal not already included in the standard Release-4 and Release-5 CSR/GFZ/JPL ocean corrections, is the global addition or subtraction of water from the ocean (the ocean models used to correct GRACE are mass-conserving), due to changes in land water/snow/ice from outside the ice sheets, and from the ice sheets themselves. Some groups included this ocean mass signal by adding/subtracting a uniform water layer to/from the oceans each month, while some distributed the extra water in a manner consistent with the self-consistent sea level equation (175). To estimate the total water volume added to the oceans, groups used GLDAS/Noah to compute globally integrated land water variability from outside the ice sheets, and used their own GRACE ice sheet estimates to find the water added to the ocean from Antarctica and Greenland.

Contamination from GIA was considered by all groups, no matter what analysis method they used. Although GIA contamination is not a serious problem for Greenland, it is arguably the largest source of uncertainty for Antarctica – and for East Antarctica, in particular. For Greenland, all participants combined results based on three ice deglaciation models: (1) Simpson et al (176), model denoted here as “Simpson”, (2) Fleming and Lambeck, (38) denoted here as “ANU”, and (3) Peltier (39) denoted here as “ICE-5G”. For Antarctica, all participants used GIA models from Whitehouse et al., (35) denoted here as W12a, Ivins et al., denoted here as IJ05\_R2, and Peltier (39) which is the same “ICE-5G” model used for Greenland. A description of how these ice deglaciation models were used to determine GRACE and altimeter corrections is provided in §4. GRACE results based on W12a and IJ05\_R2 were combined to generate mass balances of the AIS, EAIS, WAIS, and APIS as reported in the main text. GRACE results based on ICE-5G were not used for those estimates, see the main text and §4 for a discussion of this point. However, separate mass balance estimates for the AIS, EAIS, WAIS, and APIS based solely on ICE-5G were computed by each group, and the results are provided and discussed below.

Each participant was faced with the problem of how to combine results computed using different GIA models. Most of the GIA models listed above were actually provided in several versions, corresponding to different solid Earth structural models (i.e. different viscosity profiles and lithospheric thicknesses; some compressible and some incompressible). For every region, each participant found, say, a W12a result, by computing a GRACE value for every version of the W12a model. Those values were combined to construct a single W12a time series and trend, usually by splitting the difference between the maximum and minimum of the different W12a GRACE values. Results for each of the other GIA models were found similarly. Combined Antarctic results for W12a and IJ05\_R2 were found by taking the arithmetic average of the separate W12a and IJ05\_R2 results. And the arithmetic average of the Simpson, ICE-5G, and

ANU results was used for Greenland. Methods for finding the GIA-related contributions to the trend uncertainties varied between groups. In most cases, the half-width of the uncertainty interval was taken as one half of the difference between the maximum and the minimum of all GIA-corrected GRACE values, as computed for all versions of each model used to construct the trend.

GRACE time series results for each region are shown in Fig. S12. In each panel, the coloured lines are the results from the different groups, and the black line is the arithmetic average of those results. The groups did not compute uncertainties for their time series values, so there is no uncertainty associated with the average. For all Antarctic regions, time series results are given after combining only the W12a and IJ05\_R2 GIA models (not ICE-5G). For Greenland, the time series were computed by combining results for the Simpson, ICE-5G, and ANU GIA models. Note the good agreement between the results for the individual groups, particularly for Greenland and West Antarctica.

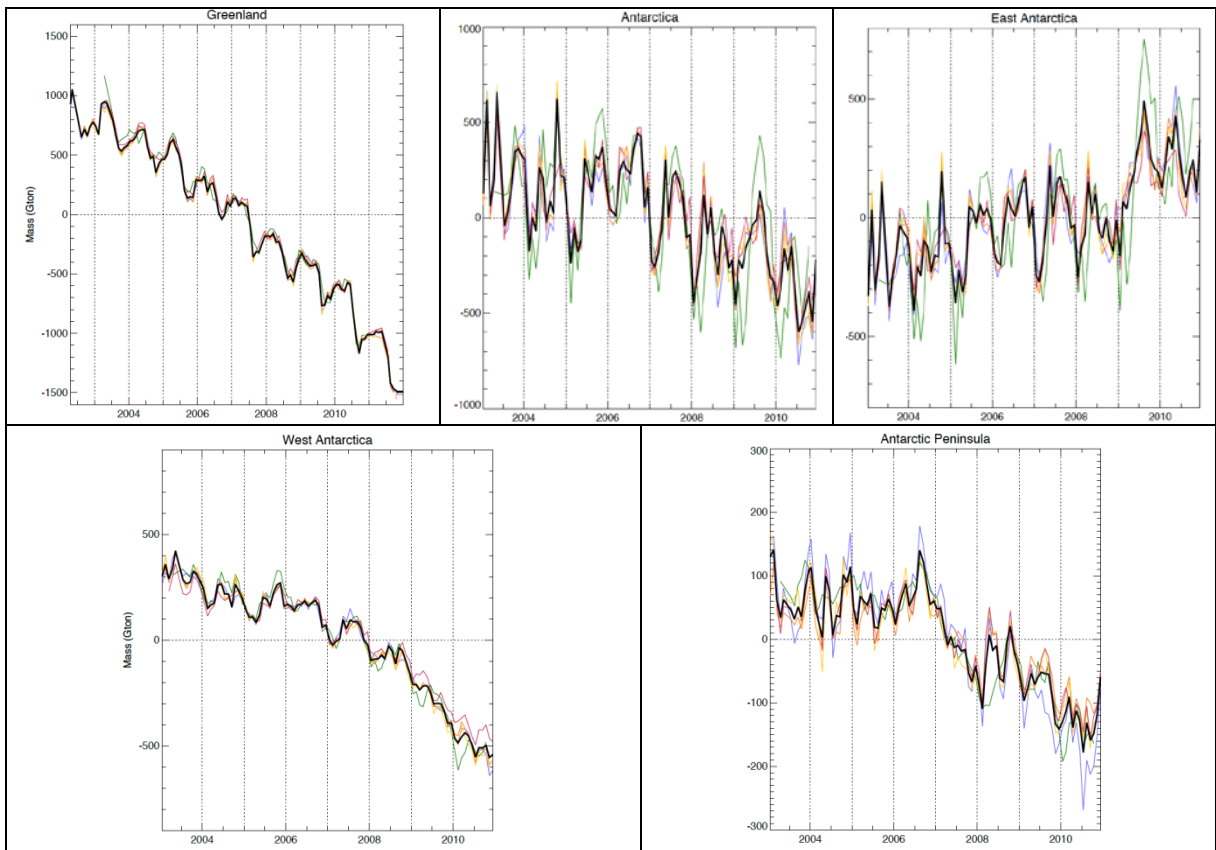


Figure S12. Monthly times series for each of the five regions. The coloured lines show the results from each individual GRACE group. The black lines show the average of those individual results.

Fig. S13 shows trends and their uncertainties for each region, for Oct, 03 – Dec, 08 and Jan, 03 – Dec, 10. Results for GrIS and AIS are also given for Jan, 05 – Dec, 10. Although each group's trends were computed by fitting to their time series values, methods for computing those trends varied. All groups fit seasonal terms simultaneously with a trend. Some groups elected to also include other terms (e.g. quadratic functions of time) in their fits. Because each group's trend uncertainties included contributions from

things besides just formal errors, those uncertainties can not be inferred from the scatter in their time series. That, plus the fact that different groups elected to fit different time-dependent functions when solving for their trends, is why each group supplied trends with uncertainties, in addition to time series values. Despite the processing differences for all involved groups we conclude that for every region, the results agree with the average GRACE estimate, to within their respective uncertainties.

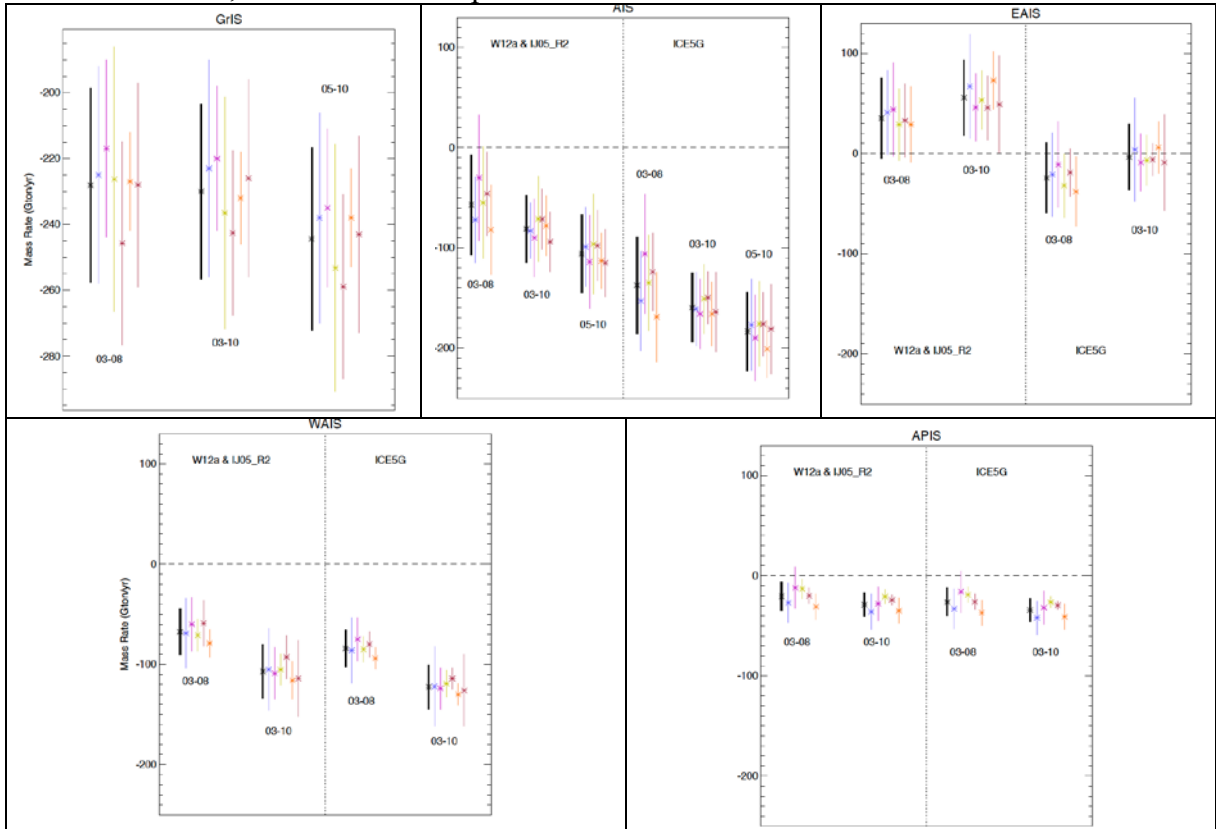


Figure S13. Trends, with uncertainties, for each of the five regions. The coloured lines show the results from each individual GRACE group. The black lines are the average of those individual results. The mid-point of the average is the average of the individual mid-points; and the width of the average uncertainty interval is the average of the individual uncertainty interval widths. Each panel shows trends for different time intervals (Jan, 03 – Dec, 10 and Oct, 03 – Dec, 08 for all regions; and Jan, 05 – Dec, 10 for GrIS and AIS). Greenland results combining the Simpson, ICE-5G, and ANU GIA models. Each Antarctic region shows results for two GIA corrections: (1) the combination of W12a and IJ05\_R2, and (2) ICE-5G. The main text lists results only for the W12a & IJ05\_R2 correction, and only for Jan, 03 – Dec, 08.

Casual readers of previously published GRACE studies may have formed the opinion that GRACE ice sheet results are heavily dependent on the analysis scheme used, and so should be regarded with some scepticism. While it is true that some of the issues that need to be addressed when processing GRACE gravity fields were not universally appreciated right away, most of the early published discrepancies were between studies that considered different time spans. Since, early-on, all those time spans were short, the best-fitting trends tended to be quite sensitive to variability that was not truly secular, which acted to increase the dependence on the time span. In the present study, a variety

of processing schemes have been used, but all have been applied to the same time span, and as Fig. S13 shows, the agreement is excellent.

Table S11 summarizes the GRACE average trends shown in Fig. S13. The main text uses results based on the W12a & IJ05\_R2 GIA models, and for the Oct, 03 – Dec, 08 time period. Note that the use of ICE-5G, instead of the W12a & IJ05\_R2 combination, increases the AIS mass loss by ~80 Gt/yr. The majority of that extra mass loss (~60 Gt/yr) occurs in the EAIS. The differences for WAIS and APIS are relatively minor. For the GrIS, the use of any one of the three GIA models alone (i.e. Simpson, ICE-5G, ANU) gives about the same trend.

Table S11. Shows final GRACE trend results, together with their uncertainties, for each region. Each trend is the arithmetic average of the trend from each GRACE group, and the width of each uncertainty interval is the arithmetic average of the uncertainty intervals from each group. Results are shown for different time spans; and, in the case of Antarctic regions, for different GIA corrections.				
Region	GIA model	Jan, 03 – Dec, 10 Gt/yr	Oct, 03 – Dec, 08 Gt/yr	Jan, 05 – Dec, 10 Gt/yr
GrIS	Simpson & ICE-5G & ANU	-230 ± 27	-228 ± 30	-244 ± 28
AIS	W12a & IJ05_R2	-81 ± 33	-57 ± 50	-106 ± 39
AIS	ICE-5G	-160 ± 34	-137 ± 49	-184 ± 40
EAIS	W12a & IJ05_R2	+56 ± 38	+35 ± 40	-
EAIS	ICE-5G	-3 ± 33	-24 ± 35	-
WAIS	W12a & IJ05_R2	-107 ± 27	-68 ± 23	-
WAIS	ICE-5G	-123 ± 22	-84 ± 18	-
APIS	W12a & IJ05_R2	-29 ± 12	-21 ± 14	-
APIS	ICE-5G	-34 ± 11	-26 ± 14	-

## References and Notes

1. J. A. Church, J. M. Gregory, in *Climate Change 2001: The Scientific Basis*, J. T. Houghton *et al.*, Eds. (Cambridge Univ. Press, Cambridge, 2001), chap. 11, pp. 641–693.
2. P. Lemke *et al.*, Changes in snow, ice and frozen ground, in *Climate Change 2007: The Physical Science Basis. Contribution of Working Group I to the Fourth Assessment Report of the Intergovernmental Panel on Climate Change*, S. Solomon *et al.*, Eds. (Cambridge Univ. Press, Cambridge, 2007), pp. 337–383.
3. A. J. Payne, A. Vieli, A. P. Shepherd, D. J. Wingham, E. Rignot, Recent dramatic thinning of largest West Antarctic ice stream triggered by oceans. *Geophys. Res. Lett.* **31**, L23401 (2004). [doi:10.1029/2004GL021284](https://doi.org/10.1029/2004GL021284)
4. C. H. Davis, Y. H. Li, J. R. McConnell, M. M. Frey, E. Hanna, Snowfall-driven growth in East Antarctic ice sheet mitigates recent sea-level rise. *Science* **308**, 1898 (2005). [doi:10.1126/science.1110662](https://doi.org/10.1126/science.1110662) [Medline](#)
5. M. van den Broeke *et al.*, Partitioning recent Greenland mass loss. *Science* **326**, 984 (2009). [doi:10.1126/science.1178176](https://doi.org/10.1126/science.1178176) [Medline](#)
6. R. G. Fairbanks, A 17,000-year glacio-eustatic sea-level record - influence of glacial melting rates on the Younger Dryas event and deep-ocean circulation. *Nature* **342**, 637 (1989). [doi:10.1038/342637a0](https://doi.org/10.1038/342637a0)
7. J. Turner *et al.*, Eds., *Antarctic Climate Change and the Environment* (Scientific Committee on Antarctic Research, Scott Polar Research Institute, Cambridge, 2009).
8. A. Shepherd *et al.*, Recent loss of floating ice and the consequent sea level contribution. *Geophys. Res. Lett.* **37**, L12502 (2010). [doi:10.1029/2010GL042496](https://doi.org/10.1029/2010GL042496)
9. A. Jenkins *et al.*, Observations beneath Pine Island Glacier in West Antarctica and implications for its retreat. *Nat. Geosci.* **3**, 468 (2010). [doi:10.1038/ngeo890](https://doi.org/10.1038/ngeo890)
10. S. S. Jacobs, A. Jenkins, C. F. Giulivi, P. Dutrieux, Stronger ocean circulation and increased melting under Pine Island Glacier ice shelf. *Nat. Geosci.* **4**, 519 (2011). [doi:10.1038/ngeo1188](https://doi.org/10.1038/ngeo1188)
11. A. Shepherd, D. J. Wingham, J. A. D. Mansley, H. F. J. Corr, Inland thinning of Pine Island Glacier, West Antarctica. *Science* **291**, 862 (2001). [doi:10.1126/science.291.5505.862](https://doi.org/10.1126/science.291.5505.862) [Medline](#)
12. D. M. Holland, R. H. Thomas, B. de Young, M. H. Ribergaard, B. Lyberth, Acceleration of Jakobshavn Isbrae triggered by warm subsurface ocean waters. *Nat. Geosci.* **1**, 659 (2008). [doi:10.1038/ngeo316](https://doi.org/10.1038/ngeo316)
13. G. A. Meehl *et al.*, Global climate projections, in *Climate Change 2007: The Physical Science Basis. Contribution of Working Group I to the Fourth Assessment Report of the Intergovernmental Panel on Climate Change*, S. Solomon *et al.*, Eds. (Cambridge Univ. Press, Cambridge, 2007), pp. 747–845.

14. E. Rignot, R. H. Thomas, Mass balance of polar ice sheets. *Science* **297**, 1502 (2002). [doi:10.1126/science.1073888](https://doi.org/10.1126/science.1073888) [Medline](#)
15. A. Shepherd, D. Wingham, Recent sea-level contributions of the Antarctic and Greenland ice sheets. *Science* **315**, 1529 (2007). [doi:10.1126/science.1136776](https://doi.org/10.1126/science.1136776) [Medline](#)
16. Further information is available at *Science* Online.
17. N. L. Bindoff *et al.*, Observations: Oceanic Climate Change and Sea Level, in *Climate Change 2007: The Physical Science Basis. Contribution of Working Group I to the Fourth Assessment Report of the Intergovernmental Panel on Climate Change*, S. Solomon *et al.*, Eds. (Cambridge Univ. Press, Cambridge, 2007).
18. E. Rignot, P. Kanagaratnam, Changes in the velocity structure of the Greenland Ice Sheet. *Science* **311**, 986 (2006). [doi:10.1126/science.1121381](https://doi.org/10.1126/science.1121381) [Medline](#)
19. A. J. Monaghan *et al.*, Insignificant change in Antarctic snowfall since the International Geophysical Year. *Science* **313**, 827 (2006). [doi:10.1126/science.1128243](https://doi.org/10.1126/science.1128243) [Medline](#)
20. I. Joughin *et al.*, Seasonal speedup along the western flank of the Greenland Ice Sheet. *Science* **320**, 781 (2008). [doi:10.1126/science.1153288](https://doi.org/10.1126/science.1153288) [Medline](#)
21. H. J. Zwally, M. B. Giovinetto, Overview and Assessment of Antarctic Ice-Sheet Mass Balance Estimates: 1992-2009. *Surv. Geophys.* **32**, 351 (2011). [doi:10.1007/s10712-011-9123-5](https://doi.org/10.1007/s10712-011-9123-5)
22. E. Van Meijgaard *et al.*, “The KNMI regional atmospheric model RACMO, version 2.1,” Technical Report 302 (2008).
23. P. K. Munneke *et al.*, A new albedo parameterization for use in climate models over the Antarctic ice sheet. *J. Geophys. Res.* **116**, D05114 (2011). [doi:10.1029/2010JD015113](https://doi.org/10.1029/2010JD015113)
24. J. Ettema *et al.*, Climate of the Greenland ice sheet using a high-resolution climate model - Part 1: Evaluation. *Cryosphere* **4**, 511 (2010). [doi:10.5194/tc-4-511-2010](https://doi.org/10.5194/tc-4-511-2010)
25. J. H. van Angelen *et al.*, Sensitivity of Greenland Ice Sheet surface mass balance to surface albedo parameterization: a study with a regional climate model. *The Cryosphere Discuss.* **6**, 1531 (2012). [doi:10.5194/tcd-6-1531-2012](https://doi.org/10.5194/tcd-6-1531-2012)
26. J. T. M. Lenaerts *et al.*, Modeling drifting snow in Antarctica with a regional climate model: 1. Methods and model evaluation. *J. Geophys. Res.* **117**, D05108 (2012). [doi:10.1029/2011JD016145](https://doi.org/10.1029/2011JD016145)
27. X. Fettweis, M. Tedesco, M. van den Broeke, J. Ettema, Melting trends over the Greenland ice sheet (1958-2009) from spaceborne microwave data and regional climate models. *Cryosphere* **5**, 359 (2011). [doi:10.5194/tc-5-359-2011](https://doi.org/10.5194/tc-5-359-2011)
28. W. J. van de Berg, thesis, Utrecht University, Utrecht, Netherlands, 2008.

29. S. R. M. Ligtenberg, M. M. Helsen, M. R. van den Broeke, An improved semi-empirical model for the densification of Antarctic firn. *Cryosphere* **5**, 809 (2011). [doi:10.5194/tc-5-809-2011](https://doi.org/10.5194/tc-5-809-2011)
30. J. Wahr, D. Wingham, C. Bentley, A method of combining ICESat and GRACE satellite data to constrain Antarctic mass balance. *J. Geophys. Res.* **105**, 16279 (2000). [doi:10.1029/2000JB900113](https://doi.org/10.1029/2000JB900113)
31. M. Bevis *et al.*, Geodetic measurements of vertical crustal velocity in West Antarctica and the implications for ice mass balance. *Geochem. Geophys. Geosyst.* **10**, Q10005 (2009). [doi:10.1029/2009GC002642](https://doi.org/10.1029/2009GC002642)
32. B. Gunter *et al.*, A comparison of coincident GRACE and ICESat data over Antarctica. *J. Geod.* **83**, 1051 (2009). [doi:10.1007/s00190-009-0323-4](https://doi.org/10.1007/s00190-009-0323-4)
33. R. E. M. Riva *et al.*, Glacial Isostatic Adjustment over Antarctica from combined ICESat and GRACE satellite data. *Earth Planet. Sci. Lett.* **288**, 516 (2009). [doi:10.1016/j.epsl.2009.10.013](https://doi.org/10.1016/j.epsl.2009.10.013)
34. I. D. Thomas *et al.*, Widespread low rates of Antarctic glacial isostatic adjustment revealed by GPS observations. *Geophys. Res. Lett.* **38**, L22302 (2011). [doi:10.1029/2011GL049277](https://doi.org/10.1029/2011GL049277)
35. P. L. Whitehouse, M. J. Bentley, G. Milne, M. King, I. Thomas, A new glacial isostatic adjustment model for Antarctica: calibrated and tested using observations of relative sea-level change and present-day uplift rates. *Geophys. J. Int.* **190**, 1464 (2012). [doi:10.1111/j.1365-246X.2012.05557.x](https://doi.org/10.1111/j.1365-246X.2012.05557.x)
36. M. J. R. Simpson, G. A. Milne, P. Huybrechts, A. J. Long, Calibrating a glaciological model of the Greenland ice sheet from the Last Glacial Maximum to present-day using field observations of relative sea level and ice extent. *Quat. Sci. Rev.* **28**, 1631 (2009). [doi:10.1016/j.quascirev.2009.03.004](https://doi.org/10.1016/j.quascirev.2009.03.004)
37. L. Tarasov, W. R. Peltier, Greenland glacial history and local geodynamic consequences. *Geophys. J. Int.* **150**, 198 (2002). [doi:10.1046/j.1365-246X.2002.01702.x](https://doi.org/10.1046/j.1365-246X.2002.01702.x)
38. K. Fleming, K. Lambeck, Constraints on the Greenland Ice Sheet since the Last Glacial Maximum from sea-level observations and glacial-rebound models. *Quat. Sci. Rev.* **23**, 1053 (2004). [doi:10.1016/j.quascirev.2003.11.001](https://doi.org/10.1016/j.quascirev.2003.11.001)
39. W. R. Peltier, Global glacial isostasy and the surface of the ice-age earth: The ice-5G (VM2) model and GRACE. *Annu. Rev. Earth Planet. Sci.* **32**, 111 (2004). [doi:10.1146/annurev.earth.32.082503.144359](https://doi.org/10.1146/annurev.earth.32.082503.144359)
40. P. L. Whitehouse, M. J. Bentley, A. M. Le Brocq, A deglacial model for Antarctica: geological constraints and glaciological modelling as a basis for a new model of Antarctic glacial isostatic adjustment. *Quat. Sci. Rev.* **32**, 1 (2012). [doi:10.1016/j.quascirev.2011.11.016](https://doi.org/10.1016/j.quascirev.2011.11.016)
41. E. R. Ivins, T. S. James, Antarctic glacial isostatic adjustment: a new assessment. *Antarct. Sci.* **17**, 541 (2005). [doi:10.1017/S0954102005002968](https://doi.org/10.1017/S0954102005002968)

42. C. Todd, J. Stone, H. Conway, B. Hall, G. Bromley, Late Quaternary evolution of Reedy Glacier, Antarctica. *Quat. Sci. Rev.* **29**, 1328 (2010).  
[doi:10.1016/j.quascirev.2010.02.001](https://doi.org/10.1016/j.quascirev.2010.02.001)
43. R. P. Ackert, Jr. *et al.*, West Antarctic Ice Sheet elevations in the Ohio Range: Geologic constraints and ice sheet modeling prior to the last highstand. *Earth Planet. Sci. Lett.* **307**, 83 (2011). [doi:10.1016/j.epsl.2011.04.015](https://doi.org/10.1016/j.epsl.2011.04.015)
44. A. S. Hein, C. J. Fogwill, D. E. Sugden, S. Xu, Glacial/interglacial ice-stream stability in the Weddell Sea embayment, Antarctica. *Earth Planet. Sci. Lett.* **307**, 211 (2011). [doi:10.1016/j.epsl.2011.04.037](https://doi.org/10.1016/j.epsl.2011.04.037)
45. A. Mackintosh *et al.*, Retreat of the East Antarctic ice sheet during the last glacial termination. *Nat. Geosci.* **4**, 195 (2011). [doi:10.1038/ngeo1061](https://doi.org/10.1038/ngeo1061)
46. O. M. Johannessen, K. Khvorostovsky, M. W. Miles, L. P. Bobylev, Recent ice-sheet growth in the interior of Greenland. *Science* **310**, 1013 (2005).  
[doi:10.1126/science.1115356](https://doi.org/10.1126/science.1115356) [Medline](#)
47. H. J. Zwally *et al.*, Mass changes of the Greenland and Antarctic ice sheets and shelves and contributions to sea-level rise: 1992-2002. *J. Glaciol.* **51**, 509 (2005).  
[doi:10.3189/172756505781829007](https://doi.org/10.3189/172756505781829007)
48. H. J. Zwally *et al.*, Greenland Ice Sheet mass balance: Distribution of increased mass loss with climate warming. *J. Glaciol.* **57**, 88 (2011).
49. D. J. Wingham, A. J. Ridout, R. Scharroo, R. J. Arthern, C. K. Shum, Antarctic elevation change from 1992 to 1996. *Science* **282**, 456 (1998).  
[doi:10.1126/science.282.5388.456](https://doi.org/10.1126/science.282.5388.456) [Medline](#)
50. D. J. Wingham, D. W. Wallis, A. Shepherd, Spatial and temporal evolution of Pine Island Glacier thinning, 1995-2006. *Geophys. Res. Lett.* **36**, L17501 (2009).  
[doi:10.1029/2009GL039126](https://doi.org/10.1029/2009GL039126)
51. J. Li, H. J. Zwally, Modeling of Firn Compaction for Estimating Ice-sheet Mass Change from Observed Ice-sheet Elevation Change. *Ann. Glaciol.* **52**, 1 (2011).  
[doi:10.3189/172756411799096321](https://doi.org/10.3189/172756411799096321)
52. D. J. Wingham, A. Shepherd, A. Muir, G. J. Marshall, Mass balance of the Antarctic ice sheet. *Philos. Trans. R. Soc. Ser. A* **364**, 1627 (2006).  
[doi:10.1098/rsta.2006.1792](https://doi.org/10.1098/rsta.2006.1792) [Medline](#)
53. H. J. Zwally, R. A. Bindshadler, A. C. Brenner, J. A. Major, J. G. Marsh, Growth of greenland ice sheet: measurement. *Science* **246**, 1587 (1989).  
[doi:10.1126/science.246.4937.1587](https://doi.org/10.1126/science.246.4937.1587) [Medline](#)
54. C. A. Shuman *et al.*, ICESat Antarctic elevation data: Preliminary precision and accuracy assessment. *Geophys. Res. Lett.* **33**, L07501 (2006).  
[doi:10.1029/2005GL025227](https://doi.org/10.1029/2005GL025227)
55. E. Rignot *et al.*, Recent Antarctic ice mass loss from radar interferometry and regional climate modelling. *Nat. Geosci.* **1**, 106 (2008). [doi:10.1038/ngeo102](https://doi.org/10.1038/ngeo102)

56. E. Rignot, J. E. Box, E. Burgess, E. Hanna, Mass balance of the Greenland ice sheet from 1958 to 2007. *Geophys. Res. Lett.* **35**, L20502 (2008).  
[doi:10.1029/2008GL035417](https://doi.org/10.1029/2008GL035417)
57. E. Rignot, I. Velicogna, M. R. van den Broeke, A. Monaghan, J. Lenaerts, Acceleration of the contribution of the Greenland and Antarctic ice sheets to sea level rise. *Geophys. Res. Lett.* **38**, L05503 (2011). [doi:10.1029/2011GL046583](https://doi.org/10.1029/2011GL046583)
58. A. Ohmura, N. Reeh, New precipitation and accumulation maps for Greenland. *J. Glaciol.* **37**, 140 (1991).
59. D. G. Vaughan, J. L. Bamber, M. Giovinetto, J. Russell, A. P. R. Cooper, Reassessment of net surface mass balance in Antarctica. *J. Clim.* **12**, 933 (1999).  
[doi:10.1175/1520-0442\(1999\)012<0933:RONSMB>2.0.CO;2](https://doi.org/10.1175/1520-0442(1999)012<0933:RONSMB>2.0.CO;2)
60. M. B. Giovinetto, H. J. Zwally, Spatial distribution of net surface accumulation on the Antarctic ice sheet. *Ann. Glaciol.* **31**, 171 (2000).  
[doi:10.3189/172756400781820200](https://doi.org/10.3189/172756400781820200)
61. J. T. M. Lenaerts, M. R. van den Broeke, W. J. van de Berg, E. van Meijgaard, P. K. Munneke, A new, high-resolution surface mass balance map of Antarctica (1979-2010) based on regional atmospheric climate modeling. *Geophys. Res. Lett.* **39**, L04501 (2012). [doi:10.1029/2011GL050713](https://doi.org/10.1029/2011GL050713)
62. I. Joughin, B. E. Smith, I. M. Howat, T. Scambos, T. Moon, Greenland flow variability from ice-sheet-wide velocity mapping. *J. Glaciol.* **56**, 415 (2010).  
[doi:10.3189/002214310792447734](https://doi.org/10.3189/002214310792447734)
63. E. Rignot, J. Mouginot, B. Scheuchl, Ice flow of the Antarctic ice sheet. *Science* **333**, 1427 (2011). [doi:10.1126/science.1208336](https://doi.org/10.1126/science.1208336) [Medline](#)
64. S. Gogineni *et al.*, Coherent radar ice thickness measurements over the Greenland ice sheet. *J. Geophys. Res.* **106**, 33761 (2001). [doi:10.1029/2001JD900183](https://doi.org/10.1029/2001JD900183)
65. I. M. Howat, I. Joughin, T. A. Scambos, Rapid changes in ice discharge from Greenland outlet glaciers. *Science* **315**, 1559 (2007).  
[doi:10.1126/science.1138478](https://doi.org/10.1126/science.1138478) [Medline](#)
66. J. Ettema *et al.*, Higher surface mass balance of the Greenland ice sheet revealed by high-resolution climate modeling. *Geophys. Res. Lett.* **36**, L12501 (2009).  
[doi:10.1029/2009GL038110](https://doi.org/10.1029/2009GL038110)
67. I. Velicogna, J. Wahr, Greenland mass balance from GRACE. *Geophys. Res. Lett.* **32**, L18505 (2005). [doi:10.1029/2005GL023955](https://doi.org/10.1029/2005GL023955)
68. S. B. Luthcke *et al.*, Recent Greenland ice mass loss by drainage system from satellite gravity observations. *Science* **314**, 1286 (2006). [doi:10.1126/science.1130776](https://doi.org/10.1126/science.1130776)  
[Medline](#)
69. J. L. Chen, C. R. Wilson, B. D. Tapley, Interannual variability of Greenland ice losses from satellite gravimetry. *J. Geophys. Res.* **116**, B07406 (2011).  
[doi:10.1029/2010JB007789](https://doi.org/10.1029/2010JB007789)

70. I. Velicogna, Increasing rates of ice mass loss from the Greenland and Antarctic ice sheets revealed by GRACE. *Geophys. Res. Lett.* **36**, L19503 (2009).  
[doi:10.1029/2009GL040222](https://doi.org/10.1029/2009GL040222)
71. B. D. Tapley, S. Bettadpur, J. C. Ries, P. F. Thompson, M. M. Watkins, GRACE measurements of mass variability in the Earth system. *Science* **305**, 503 (2004).  
[doi:10.1126/science.1099192](https://doi.org/10.1126/science.1099192) [Medline](#)
72. S. B. Luthcke, A. A. Arendt, D. D. Rowlands, J. J. McCarthy, C. F. Larsen, Recent glacier mass changes in the Gulf of Alaska region from GRACE mascon solutions. *J. Glaciol.* **54**, 767 (2008). [doi:10.3189/002214308787779933](https://doi.org/10.3189/002214308787779933)
73. E. R. Ivins *et al.*, On-land ice loss and glacial isostatic adjustment at the Drake Passage: 2003-2009. *J. Geophys. Res.* **116**, B02403 (2011).  
[doi:10.1029/2010JB007607](https://doi.org/10.1029/2010JB007607)
74. A. Shepherd, D. J. Wingham, J. A. D. Mansley, Inland thinning of the Amundsen Sea sector, West Antarctica. *Geophys. Res. Lett.* **29**, 1364 (2002).  
[doi:10.1029/2001GL014183](https://doi.org/10.1029/2001GL014183)
75. C. Boening, M. Lebsock, F. Landerer, G. Stephens, Snowfall-driven mass change on the East Antarctic ice sheet. *Geophys. Res. Lett.* **39**, L21501 (2012).
76. I. Velicogna, J. Wahr, Acceleration of Greenland ice mass loss in spring 2004. *Nature* **443**, 329 (2006). [doi:10.1038/nature05168](https://doi.org/10.1038/nature05168) [Medline](#)
77. H. D. Pritchard, R. J. Arthern, D. G. Vaughan, L. A. Edwards, Extensive dynamic thinning on the margins of the Greenland and Antarctic ice sheets. *Nature* **461**, 971 (2009). [doi:10.1038/nature08471](https://doi.org/10.1038/nature08471) [Medline](#)
78. E. Rignot *et al.*, Accelerated ice discharge from the Antarctic Peninsula following the collapse of Larsen B ice shelf. *Geophys. Res. Lett.* **31**, L18401 (2004).  
[doi:10.1029/2004GL020697](https://doi.org/10.1029/2004GL020697)
79. H. Rott, F. Müller, T. Nagler, D. Floricioiu, The imbalance of glaciers after disintegration of Larsen-B ice shelf, Antarctic Peninsula. *Cryosphere* **5**, 125 (2011). [doi:10.5194/tc-5-125-2011](https://doi.org/10.5194/tc-5-125-2011)
80. E. Berthier, T. A. Scambos, C. A. Shuman, Mass loss of Larsen B tributary glaciers (Antarctic Peninsula) unabated since 2002. *Geophys. Res. Lett.* **39**, L13501 (2012). [doi:10.1029/2012GL051755](https://doi.org/10.1029/2012GL051755)
81. W. Krabill *et al.*, Greenland Ice Sheet: Increased coastal thinning. *Geophys. Res. Lett.* **31**, L24402 (2004). [doi:10.1029/2004GL021533](https://doi.org/10.1029/2004GL021533)
82. I. Velicogna, J. Wahr, Measurements of time-variable gravity show mass loss in Antarctica. *Science* **311**, 1754 (2006). [doi:10.1126/science.1123785](https://doi.org/10.1126/science.1123785) [Medline](#)
83. I. Joughin, W. Abdalati, M. Fahnestock, Large fluctuations in speed on Greenland's Jakobshavn Isbrae glacier. *Nature* **432**, 608 (2004). [doi:10.1038/nature03130](https://doi.org/10.1038/nature03130)  
[Medline](#)
84. E. J. O. Schrama, B. Wouters, Revisiting Greenland ice sheet mass loss observed by GRACE. *J. Geophys. Res.* **116**, B02407 (2011). [doi:10.1029/2009JB006847](https://doi.org/10.1029/2009JB006847)

85. T. Moon, I. Joughin, B. Smith, I. Howat, 21st-century evolution of Greenland outlet glacier velocities. *Science* **336**, 576 (2012). [doi:10.1126/science.1219985](https://doi.org/10.1126/science.1219985) [Medline](#)
86. M. Tedesco *et al.*, The role of albedo and accumulation in the 2010 melting record in Greenland. *Environ. Res. Lett.* **6**, 014005 (2011). [doi:10.1088/1748-9326/6/1/014005](https://doi.org/10.1088/1748-9326/6/1/014005)
87. H. Rott, P. Skvarca, T. Nagler, Rapid collapse of northern Larsen Ice Shelf. *Antarct. Sci.* **271**, 788 (1996).
88. H. De Angelis, P. Skvarca, Glacier surge after ice shelf collapse. *Science* **299**, 1560 (2003). [doi:10.1126/science.1077987](https://doi.org/10.1126/science.1077987) [Medline](#)
89. A. J. Cook, A. J. Fox, D. G. Vaughan, J. G. Ferrigno, Retreating glacier fronts on the Antarctic Peninsula over the past half-century. *Science* **308**, 541 (2005). [doi:10.1126/science.1104235](https://doi.org/10.1126/science.1104235) [Medline](#)
90. I. Goodwin, M. de Angelis, M. Pook, N. W. Young, Snow accumulation variability in Wilkes Land, East Antarctica, and the relationship to atmospheric ridging in the 130 degrees-170 degrees E region since 1930. *J. Geophys. Res.* **108**, 16 (2003). [doi:10.1029/2002JD002995](https://doi.org/10.1029/2002JD002995)
91. P. Uotila, A. H. Lynch, J. J. Cassano, R. I. Cullather, Changes in Antarctic net precipitation in the 21st century based on Intergovernmental Panel on Climate Change (IPCC) model scenarios. *J. Geophys. Res.* **112**, D10107 (2007). [doi:10.1029/2006JD007482](https://doi.org/10.1029/2006JD007482)
92. G. Krinner, O. Magand, I. Simmonds, C. Genthon, J. L. Dufresne, Simulated Antarctic precipitation and surface mass balance at the end of the twentieth and twenty-first centuries. *Clim. Dyn.* **28**, 215 (2007). [doi:10.1007/s00382-006-0177-x](https://doi.org/10.1007/s00382-006-0177-x)
93. T. J. Bracegirdle, W. M. Connolley, J. Turner, Antarctic climate change over the twenty first century. *J. Geophys. Res.* **113**, D03103 (2008). [doi:10.1029/2007JD008933](https://doi.org/10.1029/2007JD008933)
94. R. Hock, M. de Woul, V. Radic, M. Dyurgerov, Mountain glaciers and ice caps around Antarctica make a large sea-level rise contribution. *Geophys. Res. Lett.* **36**, L07501 (2009). [doi:10.1029/2008GL037020](https://doi.org/10.1029/2008GL037020)
95. G. Heiss, D. Vaughan, Ice2sea review of published ice-sheet mass-balance estimates. Ice2sea Internal Deliverable (2011).
96. W. Krabill *et al.*, Greenland ice sheet: High-elevation balance and peripheral thinning. *Science* **289**, 428 (2000). [doi:10.1126/science.289.5478.428](https://doi.org/10.1126/science.289.5478.428) [Medline](#)
97. J. L. Chen, C. R. Wilson, D. D. Blankenship, B. D. Tapley, Antarctic mass rates from GRACE. *Geophys. Res. Lett.* **33**, L11502 (2006). [doi:10.1029/2006GL026369](https://doi.org/10.1029/2006GL026369)
98. G. Ramillien *et al.*, Interannual variations of the mass balance of the Antarctica and Greenland ice sheets from GRACE. *Global Planet. Change* **53**, 198 (2006). [doi:10.1016/j.gloplacha.2006.06.003](https://doi.org/10.1016/j.gloplacha.2006.06.003)

99. R. Thomas, E. Frederick, W. Krabill, S. Manizade, C. Martin, Progressive increase in ice loss from Greenland. *Geophys. Res. Lett.* **33**, L10503 (2006).  
[doi:10.1029/2006GL026075](https://doi.org/10.1029/2006GL026075)
100. R. Forsberg, N. Reeh, Mass change of the Greenland Ice Sheet from GRACE, in *Gravity Field of the Earth, Proceedings of the 1st Meeting of the International Gravity Field Service* (Harita Dergisi, Ankara, 2007), vol. 73, issue 18 (revised version).
101. B. Wouters, D. Chambers, E. J. O. Schrama, GRACE observes small-scale mass loss in Greenland. *Geophys. Res. Lett.* **35**, L20501 (2008).  
[doi:10.1029/2008GL034816](https://doi.org/10.1029/2008GL034816)
102. V. R. Barletta, R. Sabadini, A. Bordoni, Isolating the PGR signal in the GRACE data: impact on mass balance estimates in Antarctica and Greenland. *Geophys. J. Int.* **172**, 18 (2008). [doi:10.1111/j.1365-246X.2007.03630.x](https://doi.org/10.1111/j.1365-246X.2007.03630.x)
103. A. Cazenave *et al.*, Sea level budget over 2003-2008: A reevaluation from GRACE space gravimetry, satellite altimetry and Argo. *Global Planet. Change* **65**, 83 (2009). [doi:10.1016/j.gloplacha.2008.10.004](https://doi.org/10.1016/j.gloplacha.2008.10.004)
104. J. L. Chen, C. R. Wilson, D. Blankenship, B. D. Tapley, Accelerated Antarctic ice loss from satellite gravity measurements. *Nat. Geosci.* **2**, 859 (2009).  
[doi:10.1038/ngeo694](https://doi.org/10.1038/ngeo694)
105. M. Horwath, R. Dietrich, Signal and error in mass change inferences from GRACE: the case of Antarctica. *Geophys. J. Int.* **177**, 849 (2009). [doi:10.1111/j.1365-246X.2009.04139.x](https://doi.org/10.1111/j.1365-246X.2009.04139.x)
106. D. C. Slobbe, P. Ditmar, R. C. Lindenbergh, Estimating the rates of mass change, ice volume change and snow volume change in Greenland from ICESat and GRACE data. *Geophys. J. Int.* **176**, 95 (2009). [doi:10.1111/j.1365-246X.2008.03978.x](https://doi.org/10.1111/j.1365-246X.2008.03978.x)
107. X. Wu *et al.*, Simultaneous estimation of global present-day water transport and glacial isostatic adjustment. *Nat. Geosci.* **3**, 642 (2010). [doi:10.1038/ngeo938](https://doi.org/10.1038/ngeo938)
108. H.-L. Shi *et al.*, Mass change detection in Antarctic ice sheet using ICESat block analysis techniques from 2003 similar to 2008. *Chin. J. Geophys. Chin. Ed.* **54**, 958 (2011).
109. L. S. Sørensen *et al.*, Mass balance of the Greenland ice sheet (2003-2008) from ICESat data - the impact of interpolation, sampling and firn density. *Cryosphere* **5**, 173 (2011). [doi:10.5194/tc-5-173-2011](https://doi.org/10.5194/tc-5-173-2011)
110. H. J. Zwally *et al.*, Greenland ice sheet mass balance: distribution of increased mass loss with climate warming; 2003-07 versus 1992-2002. *J. Glaciol.* **57**, 88 (2011).  
[doi:10.3189/002214311795306682](https://doi.org/10.3189/002214311795306682)
111. M. B. Giovinetto, R. Bentley, Surface balance in ice drainage systems of Antarctica. *Antarct. J. U.S.* **20**, 6 (1985).

112. D. J. Drewry, The surface of the Antarctic ice sheet, in *Antarctica: Glaciological and Geophysical Folio*, D. J. Drewry, Ed., (Scott Polar Research Institute, University of Cambridge, Cambridge, 1983), Sheet 2.
113. H. J. Zwally, M. B. Giovinetto, M. A. Beckley, J. L. Saba, Antarctic and Greenland Drainage Systems, GSFC Cryospheric Sciences Laboratory, at [http://icesat4.gsfc.nasa.gov/cryo\\_data/ant\\_grn\\_drainage\\_systems.php](http://icesat4.gsfc.nasa.gov/cryo_data/ant_grn_drainage_systems.php) (2012).
114. H. J. Zwally *et al.*, ICESat's laser measurements of polar ice, atmosphere, ocean, and land. *J. Geodyn.* **34**, 405 (2002).
115. J. DiMarzio, A. Brenner, R. Schutz, C. A. Shuman, H. J. Zwally. GLAS/ICESat 1 km laser altimetry digital elevation model of Greenland (National Snow and Ice Data Center, Boulder, CO, 2007).
116. B. M. Csatho, A. F. Schenk, C. J. van der Veen, W. B. Krabill. Reconstruction of Greenland Ice Sheet changes from laser altimetry measurements. *Eos Trans. AGU* **90** (fall meeting suppl.), abstr. no. G52A-04 (2009); [webserv.cs.umt.edu/isis/index.php/Present\\_Day\\_Greenland](http://webserv.cs.umt.edu/isis/index.php/Present_Day_Greenland).
117. D. P. Dee *et al.*, The ERA-Interim reanalysis: configuration and performance of the data assimilation system. *Q. J. R. Meteorol. Soc.* **137**, 553 (2011). [doi:10.1002/qj.828](https://doi.org/10.1002/qj.828)
118. S. Saha *et al.*, The NCEP climate forecast system reanalysis. *Bull. Am. Meteorol. Soc.* **91**, 1015 (2010). [doi:10.1175/2010BAMS3001.1](https://doi.org/10.1175/2010BAMS3001.1)
119. M. M. Rienecker *et al.*, MERRA: NASA's Modern-Era Retrospective Analysis for Research and Applications. *J. Clim.* **24**, 3624 (2011). [doi:10.1175/JCLI-D-11-00015.1](https://doi.org/10.1175/JCLI-D-11-00015.1)
120. L. Bengtsson, S. Hagemann, K. I. Hodges, Can climate trends be calculated from reanalysis data? *J. Geophys. Res.* **109**, D11111 (2004). [doi:10.1029/2004JD004536](https://doi.org/10.1029/2004JD004536)
121. D. H. Bromwich, R. L. Fogt, K. I. Hodges, J. E. Walsh, A tropospheric assessment of the ERA-40, NCEP, and JRA-25 global reanalyses in the polar regions. *J. Geophys. Res.* **112**, D10111 (2007). [doi:10.1029/2006JD007859](https://doi.org/10.1029/2006JD007859)
122. D. H. Bromwich, J. P. Nicolas, A. J. Monaghan, An Assessment of Precipitation Changes over Antarctica and the Southern Ocean since 1989 in Contemporary Global Reanalyses. *J. Clim.* **24**, 4189 (2011). [doi:10.1175/2011JCLI4074.1](https://doi.org/10.1175/2011JCLI4074.1)
123. K. E. Trenberth, J. T. Fasullo, J. Mackaro, Atmospheric Moisture Transports from Ocean to Land and Global Energy Flows in Reanalyses. *J. Clim.* **24**, 4907 (2011). [doi:10.1175/2011JCLI4171.1](https://doi.org/10.1175/2011JCLI4171.1)
124. J. P. Nicolas, D. H. Bromwich, Precipitation Changes in High Southern Latitudes from Global Reanalyses: A Cautionary Tale. *Surv. Geophys.* **32**, 475 (2011). [doi:10.1007/s10712-011-9114-6](https://doi.org/10.1007/s10712-011-9114-6)
125. R. I. Cullather, M. G. Bosilovich, The Moisture Budget of the Polar Atmosphere in MERRA. *J. Clim.* **24**, 2861 (2011). [doi:10.1175/2010JCLI4090.1](https://doi.org/10.1175/2010JCLI4090.1)

126. F. R. Robertson, M. G. Bosilovich, J. Chen, T. L. Miller, The Effect of Satellite Observing System Changes on MERRA Water and Energy Fluxes. *J. Clim.* **24**, 5197 (2011). [doi:10.1175/2011JCLI4227.1](https://doi.org/10.1175/2011JCLI4227.1)
127. A. J. Monaghan, D. H. Bromwich, Advances describing recent Antarctic climate variability. *Bull. Am. Meteorol. Soc.* **89**, 1295 (2008). [doi:10.1175/2008BAMS2543.1](https://doi.org/10.1175/2008BAMS2543.1)
128. B. L. Hall, T. Koffman, G. H. Denton, Reduced ice extent on the western Antarctic Peninsula at 700-970 cal. yr BP. *Geology* **38**, 635 (2010). [doi:10.1130/G30932.1](https://doi.org/10.1130/G30932.1)
129. A. R. Simms, E. R. Ivins, R. DeWitt, P. Kouremenos, L. M. Simkins, Timing of the most recent Neoglacial advance and retreat in the South Shetland Islands, Antarctic Peninsula: Insights from raised beaches and Holocene uplift rates. *Quat. Sci. Rev.* **47**, 41 (2012). [doi:10.1016/j.quascirev.2012.05.013](https://doi.org/10.1016/j.quascirev.2012.05.013)
130. J. Bentley *et al.*, Deglacial history of the West Antarctic Ice Sheet in the Weddell Sea embayment: Constraints on past ice volume change. *Geology* **38**, 411 (2010). [doi:10.1130/G30754.1](https://doi.org/10.1130/G30754.1)
131. D. Buiron *et al.*, TALDICE-1 age scale of the Talos Dome deep ice core, East Antarctica. *Climate Past* **7**, 1 (2011). [doi:10.5194/cp-7-1-2011](https://doi.org/10.5194/cp-7-1-2011)
132. T. S. James, E. R. Ivins, Predictions of Antarctic crustal motions driven by present-day ice sheet evolution and by isostatic memory of the Last Glacial Maximum. *J. Geophys. Res.* **103**, 4993 (1998). [doi:10.1029/97JB03539](https://doi.org/10.1029/97JB03539)
133. K. M. Simon, T. S. James, E. R. Ivins, Ocean loading effects on the prediction of Antarctic glacial isostatic uplift and gravity rates. *J. Geod.* **84**, 305 (2010). [doi:10.1007/s00190-010-0368-4](https://doi.org/10.1007/s00190-010-0368-4)
134. A. M. Le Brocq *et al.*, Reconstructing the Last Glacial Maximum ice sheet in the Weddell Sea embayment, Antarctica, using numerical modelling constrained by field evidence. *Quat. Sci. Rev.* **30**, 2422 (2011). [doi:10.1016/j.quascirev.2011.05.009](https://doi.org/10.1016/j.quascirev.2011.05.009)
135. I. C. Rutt, M. Hagdorn, N. R. J. Hulton, A. J. Payne, The Glimmer community ice sheet model. *J. Geophys. Res.* **114**, F02004 (2009). [doi:10.1029/2008JF001015](https://doi.org/10.1029/2008JF001015)
136. J. B. Anderson, S. S. Shipp, A. L. Lowe, J. S. Wellner, A. B. Mosola, The Antarctic Ice Sheet during the Last Glacial Maximum and its subsequent retreat history: a review. *Quat. Sci. Rev.* **21**, 49 (2002). [doi:10.1016/S0277-3791\(01\)00083-X](https://doi.org/10.1016/S0277-3791(01)00083-X)
137. F. Parrenin *et al.*, 1-D-ice flow modelling at EPICA Dome C and Dome Fuji, East Antarctica. *Climate Past* **3**, 243 (2007). [doi:10.5194/cp-3-243-2007](https://doi.org/10.5194/cp-3-243-2007)
138. T. A. Neumann *et al.*, Holocene accumulation and ice sheet dynamics in central West Antarctica. *J. Geophys. Res.* **113**, F02018 (2008). [doi:10.1029/2007JF000764](https://doi.org/10.1029/2007JF000764)
139. E. Verleyen *et al.*, Post-glacial regional climate variability along the East Antarctic coastal margin-Evidence from shallow marine and coastal terrestrial records. *Earth Sci. Rev.* **104**, 199 (2011). [doi:10.1016/j.earscirev.2010.10.006](https://doi.org/10.1016/j.earscirev.2010.10.006)

140. D. A. White, D. Fink, D. B. Gore, Cosmogenic nuclide evidence for enhanced sensitivity of an East Antarctic ice stream to change during the last deglaciation. *Geology* **39**, 23 (2011). [doi:10.1130/G31591.1](https://doi.org/10.1130/G31591.1)
141. M. Siddall, G. A. Milne, V. Masson-Delmotte, Uncertainties in elevation changes and their impact on Antarctic temperature records since the end of the last glacial period. *Earth Planet. Sci. Lett.* **315-316**, L16401 (2012). [doi:10.1016/j.epsl.2011.04.032](https://doi.org/10.1016/j.epsl.2011.04.032)
142. K. Lambeck *et al.*, Sea level and shoreline reconstructions for the Red Sea: isostatic and tectonic considerations and implications for hominin migration out of Africa. *Quat. Sci. Rev.* **30**, 3542 (2011). [doi:10.1016/j.quascirev.2011.08.008](https://doi.org/10.1016/j.quascirev.2011.08.008)
143. G. Balco, Contributions and unrealized potential contributions of cosmogenic-nuclide exposure dating to glacier chronology, 1990-2010. *Quat. Sci. Rev.* **30**, 3 (2011). [doi:10.1016/j.quascirev.2010.11.003](https://doi.org/10.1016/j.quascirev.2010.11.003)
144. E. R. Ivins, C. G. Sammis, C. F. Yoder, Deepmantle viscous structure with prior estimate and satellite constraint. *J. Geophys. Res.* **98**, 4579 (1993). [doi:10.1029/92JB02728](https://doi.org/10.1029/92JB02728)
145. L. Hanyk, D. A. Yuen, C. Matyska, Initial-value and modal approaches for transient viscoelastic responses with complex viscosity profiles. *Geophys. J. Int.* **127**, 348 (1996). [doi:10.1111/j.1365-246X.1996.tb04725.x](https://doi.org/10.1111/j.1365-246X.1996.tb04725.x)
146. J. X. Mitrovica, G. A. Milne, On post-glacial sea level: I. General theory. *Geophys. J. Int.* **154**, 253 (2003). [doi:10.1046/j.1365-246X.2003.01942.x](https://doi.org/10.1046/j.1365-246X.2003.01942.x)
147. J. X. Mitrovica, J. Wahr, Ice Age Earth Rotation. *Annu. Rev. Earth Planet. Sci.* **39**, 577 (2011). [doi:10.1146/annurev-earth-040610-133404](https://doi.org/10.1146/annurev-earth-040610-133404)
148. A. Paulson, S. Zhong, J. Wahr, Inference of mantle viscosity from GRACE and relative sea level data. *Geophys. J. Int.* **171**, 497 (2007). [doi:10.1111/j.1365-246X.2007.03556.x](https://doi.org/10.1111/j.1365-246X.2007.03556.x)
149. S. Swenson, J. Wahr, Multi-sensor analysis of water storage variations of the Caspian Sea. *Geophys. Res. Lett.* **34**, L23402 (2007). [doi:10.1029/2007GL030733](https://doi.org/10.1029/2007GL030733)
150. P. Moore, M. A. King, Antarctic ice mass balance estimates from GRACE: Tidal aliasing effects. *J. Geophys. Res.* **113**, F02005 (2008). [doi:10.1029/2007JF000871](https://doi.org/10.1029/2007JF000871)
151. R. D. Ray, S. B. Luthcke, J. P. Boy, Qualitative comparisons of global ocean tide models by analysis of intersatellite ranging data. *J. Geophys. Res. Oceans* **114**, C09017 (2009). [doi:10.1029/2009JC005362](https://doi.org/10.1029/2009JC005362)
152. T. J. J. Hanebuth, K. Statterger, A. Bojanowski, Termination of the Last Glacial Maximum sea-level lowstand: The Sunda-Shelf data revisited. *Global Planet. Change* **66**, 76 (2009). [doi:10.1016/j.gloplacha.2008.03.011](https://doi.org/10.1016/j.gloplacha.2008.03.011)
153. R. J. Arthern, D. J. Wingham, The natural fluctuations of firn densification and their effect on the geodetic determination of ice sheet mass balance. *Clim. Change* **40**, 605 (1998). [doi:10.1023/A:1005320713306](https://doi.org/10.1023/A:1005320713306)

154. S. Anandakrishnan, R. B. Alley, Stagnation of ice stream C, West Antarctica by water piracy. *Geophys. Res. Lett.* **24**, 265 (1997). [doi:10.1029/96GL04016](https://doi.org/10.1029/96GL04016)
155. E. Mosley-Thompson *et al.*, Glaciological studies at Siple Station (antarctica) - potential ice-core paleoclimatic record. *J. Glaciol.* **37**, 11 (1991).
156. A. Gow, Technical Report 78 (Corps of Engineers, U.S. Army Cold Regions Research and Engineering Laboratory, Hanover, NH, 1961).
157. R. L. Cameron, in *Antarctic Snow and Ice Studies*, vol. 2 of *Antarctic Research Series*, M. Mellor, Ed. (American Geophysical Union, Washington, DC, 1964), pp. 1–31.
158. M. B. Giovinetto, W. Schwerdtfeger, *Arch. Meteorol. Geophys. Bioklimatol. Ser. A* **15**, 227 (1966).
159. R. M. Koerner, in *Antarctic Snow and Ice Studies II*, vol. 16 of *Antarctic Research Series*, A, P. Crary, Ed. (American Geophysical Union, Washington, DC, 1971), pp. 225–238.
160. E. Isaksson *et al.*, A century of accumulation and temperature changes in Dronning Maud Land, Antarctica. *J. Geophys. Res.* **101**, 7085 (1996). [doi:10.1029/95JD03232](https://doi.org/10.1029/95JD03232)
161. H. D. Pritchard *et al.*, Antarctic ice-sheet loss driven by basal melting of ice shelves. *Nature* **484**, 502 (2012). [doi:10.1038/nature10968](https://doi.org/10.1038/nature10968) [Medline](#)
162. O. B. Christensen *et al.*, The HIRHAM Regional Climate Model. Version 5, Technical Report 06-17, DMI technical report (Cambridge Univ. Press, Cambridge, 2006); available at [www.dmi.dk/dmi/tr06-17.pdf](http://www.dmi.dk/dmi/tr06-17.pdf).
163. B. E. Smith, H. A. Fricker, I. R. Joughin, S. Tulaczyk, An inventory of active subglacial lakes in Antarctica detected by ICESat (2003-2008). *J. Glaciol.* **55**, 573 (2009). [doi:10.3189/002214309789470879](https://doi.org/10.3189/002214309789470879)
164. E. Rignot, J. Mouginot, B. Scheuchl, Antarctic grounding line mapping from differential satellite radar interferometry. *Geophys. Res. Lett.* **38**, L10504 (2011). [doi:10.1029/2011GL047109](https://doi.org/10.1029/2011GL047109)
165. T. A. Scambos, T. M. Haran, M. A. Fahnestock, T. H. Painter, J. Bohlander, MODIS-based Mosaic of Antarctica (MOA) datasets: continent-wide surface morphology and snow grain size. *Remote Sens. Environ.* **111**, 242 (2007). [doi:10.1016/j.rse.2006.12.020](https://doi.org/10.1016/j.rse.2006.12.020)
166. P. Gogineni, CReSIS Greenland and Antarctic Data, Lawrence, KS, <http://data.cresis.ku.edu/> (2012).
167. C. Leuschen, *IceBridge MCoRDS LIB Geolocated Radar Echo Strength Profiles*, version 1.3 [NASA Distributed Active Archive Center at National Snow and Ice Data Center (NSIDC), Boulder, CO, 2011].
168. D. D. Blankenship, S. Kempf, D. Young, *IceBridge HiCARS 2 L2 Geolocated Ice Thickness*, version 1.0 (NASA Distributed Active Archive Center at NSIDC, Boulder, CO, 2012).

169. M. B. Lythe, D. G. Vaughan, BEDMAP: a new ice thickness and subglacial topographic model of Antarctica. *J. Geophys. Res.* **106**, 11335 (2001). [doi:10.1029/2000JB900449](https://doi.org/10.1029/2000JB900449)
170. J. A. Griggs, J. L. Bamber, Antarctic ice-shelf thickness from satellite radar altimetry. *J. Glaciol.* **57**, 485 (2011). [doi:10.3189/002214311796905659](https://doi.org/10.3189/002214311796905659)
171. E. Rignot, J. Mouginot, Ice flow in Greenland for the International Polar Year 2008-2009. *Geophys. Res. Lett.* **39**, L11501 (2012). [doi:10.1029/2012GL051634](https://doi.org/10.1029/2012GL051634)
172. L. S. Sørensen, R. Forsberg, Greenland Ice Sheet Mass Loss from GRACE Monthly Models. *Gravity Geoid Earth Obs.* **135**, 527 (2010). [doi:10.1007/978-3-642-10634-7\\_70](https://doi.org/10.1007/978-3-642-10634-7_70)
173. V. R. Barletta, L. S. S. Sørensen, R. Forsberg, Variability of mass changes at basin scale for Greenland and Antarctica. *Cryosphere Discuss.* **6**, 3397 (2012). [doi:10.5194/tcd-6-3397-2012](https://doi.org/10.5194/tcd-6-3397-2012)
174. M. Rodell *et al.*, The global land data assimilation system. *Bull. Am. Meteorol. Soc.* **85**, 381 (2004). [doi:10.1175/BAMS-85-3-381](https://doi.org/10.1175/BAMS-85-3-381)
175. M. E. Tamisiea, J. X. Mitrovica, G. A. Milne, J. L. Davis, Global geoid and sea level changes due to present-day ice mass fluctuations. *J. Geophys. Res.* **106**, 30849 (2001). [doi:10.1029/2000JB000011](https://doi.org/10.1029/2000JB000011)
176. M. J. R. Simpson, G. A. Milne, P. Huybrechts, A. J. Long, Calibrating a glaciological model of the Greenland ice sheet from the Last Glacial Maximum to present-day using field observations of relative sea level and ice extent. *Quat. Sci. Rev.* **28**, 1631 (2009). [doi:10.1016/j.quascirev.2009.03.004](https://doi.org/10.1016/j.quascirev.2009.03.004)